Shot noise measurements at single atom contacts in a low-temperature Scanning tunnelling microscope

Dissertation

zur Erlangung des Doktorgrades
der Mathematisch-Naturwissenschaftlichen Fakultät
der Christian-Albrechts-Universität zu Kiel
vorgelegt von

Andreas Burtzlaff

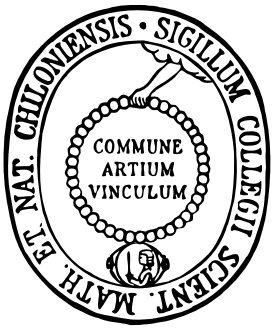

Kiel, 2017

Erster Gutachter:	Prof. Dr. Richard Berndt
Zweiter Gutachter:	Prof. Dr. Michael Bauer
Tag der mündlichen Prüfung:	31.5.2017
Zum Druck genehmigt:	31.5.2017

Contents

Abstract

In this thesis a setup for measuring shot noise at contacts formed inside a low temperature scanning tunnelling microscope (LT-STM) was developed. Such noise measurements were performed for contacts to single Au, Co and Fe atoms on a Au(111) surface. The results were used to examine the transport channels involved in the transport process and identify a spin-polarisation in the transport through the Co and Fe atoms.

Atomic contacts can be formed inside a LT-STM with a high degree of control on the contact geometry and its surroundings. To gain information on the transport properties of a contact the usual approach is to measure the conductance as well as the differential conductance. Yet from these quantities alone deductions on the transport channels and their transmissivities τ_i are only limited, since they are related to the sum $\sum_i \tau_i$ only. In contrast, the shot noise generated by the contact under bias depends on the transmissivities in a non-linear way and can thus yield definite information on the transmission channels. While shot noise can yield valuable information its measurement poses high demands on the measurement apparatus since its magnitude is comparable or even smaller than the input noise of the amplifiers. The voltage noise generated by the contact under constant current bias was measured using two home-built amplifiers in parallel. To suppress the correlated noise contribution including the amplifiers input voltage noise the cross-spectra of the two signals are calculated and averaged.

For the contacts to Au atoms a noise suppression was found that coincides with a single non-polarised channel thereby reproducing prior measurements in mechanically controlled break junction setup. Some of the contacts to Co and Fe atoms showed a noise reduction that can only be explained within the model used by assuming a spin-polarisation of the transport channels. Transport calculations performed by Mads Brandbyge reproduce these results and identify a single dominating transport channel with d_z^2 character.

To the best of my knowledge the shot noise measurements presented in this thesis are the first to be performed at atomic contacts inside an LT-STM.

Zusammenfassung

In dieser Arbeit wurde ein Messaufbau entwickelt, mit dem das Schrotrauschen von Kontakten, die in einem Tieftemperatur Raster-Tunnel-Mikroskop (TT-STM) erzeugt werden, gemessen werden kann. Rauschmessungen wurden an Einzelatomkontakten von Au, Co und Fe auf einer Au(111) Oberfläche durchgeführt. Aus den Messergebnissen konnten Aussagen über die am Transportprozess beteiligten Transportkanäle gemacht werden, sowie für den Transport durch Co- und Fe-Atome eine Spinpolarisation der Transportzustände nachgewiesen werden.

Ein LT-STM ermöglicht das kontrollierte Kontaktieren einzelner Atome auf Oberflächen und bietet vielfältige Möglichkeiten zur Charakterisierung des Kontaktes sowie seiner Umgebung. Die übliche Methode um Kenntnisse über die Transporteigenschaften des Kontaktes zu erlangen ist die Messung des Leitwertes sowie des differentiellen Leitwertes. Aus diesen Messgrößen allein sind Rückschlüsse auf die Transportkanäle sowie die Transmissivitäten nur sehr bedingt möglich, weil sie lediglich von der Summe $\sum_i \tau_i$ abhängen. Das Schrotrauschen, das vom Kontakt erzeugt wird, hingegen hängt über einen nicht-linearen Ausdruck, dem Fano-Faktor, von den Transmissivitäten ab und lässt somit auf die Anzahl der beteiligten Transportkanäle sowie deren Spinpolarisation schließen. Die Messung des Schrotrauschens stellt hohe Anforderungen an den Messaufbau, weil seine Amplitude in der gleichen Grössenordnung oder sogar unter dem Eingangsrauschen der Verstärker liegt. Durch den Kontakt wird ein konstanter Strom geleitet und das entstehende Spannungrauschen mit zwei Verstärkern gleichzeitig gemessen. Um die korrelierten Rauschanteile insbesondere der Verstärker zu unterdrücken, wird das Kreuz-Spektrum der beiden Signale gemittelt.

Die Messungen an einzelnen Au Atomen ergaben eine Unterdrückung des Schrotrauschen, welches mit den Erwartungen für einen einzelnen nicht spinpolarisierten Kanal übereinstimmt und vorangehende Messungen reproduziert. Die Kontakte zu den Co und Fe Atomen zeigten in einigen Fällen eine Verringerung des Schrotrauschens, wie sie im Rahmen des verwendeten Modells nur durch eine Spinpolarisation der beteiligten Transportkanäle zu erklären ist. Transportrech-

nungen der Co und Fe Systeme reproduzieren dieses Verhalten und identifizieren in beiden Fällen einen einzelnen d_z^2-artigen Transportkanal als dominierend.

Meines Wissens sind die durchgeführten Messungen die ersten, die an atomaren Kontakten in einem TT-STM durchgeführt wurden.

1. Introduction

Electronic charge transport in solid state systems has proven to be a most versatile means of building those information processing and sensoric devices, that underlie our modern information society. In the endeavour to constantly increase the performance and lower the power consumption of these devices, heat dissipation is the main obstacle that requires a constant reduction in size. The minimal entity conceivable in this context as both conductor and functional element is a single atom. Therefore, the availablity of techniques such as scanning tunnelling microscopy (STM) and mechanically controlled break junction (MCBJ) to build and examine single atom contacts and atomic chains has sparked intense scientific activity to reveal their electronic transport properties [1].

Concurrently, progress on the theoretical side has filtered out a prevailing model where the ballistic transport is governed by a set of independent conduction channels. Each channel can contribute a maximum of one quantum of conductance G_0 to the total conductance and its contribution is reduced by the channel's transmissivity τ. Though the conductance is the obvious first choice in assessing the transport process due to its ease of measurement, the information it yields is severely limited since it depends on the sum $\sum_n \tau_n$ of the transmissivities only.

Shot noise measurements have proven to be a pivotal progress that augments the accessible information on the transport process [2]. In contrast to the conductance, the Fano factor, i.e. the linear coefficient connecting the shot noise power density generated by the contact with the applied bias current, has a nonlinear dependency on the transmissivities τ. Its measurement therefore enables deductions on the number of transmission channels participating in the transport process, their transmissivities τ_n and even their spin polarisation, as will be elucidated in the first chapter of this thesis. In particular, the possibility of probing spin-polarisation of the transport channels without requiring a spin-polarisation of tip or substrat makes shot noise measurements a unique analysis technique for magnetic systems. In this thesis spin-polarisation of the transport channels was successfully probed for single Co and Fe adatoms on a Au(111) surface contacted

with a Au tip.

The use of shot noise measurements to gain information on the transmission channels of mesoscopic systems was pioneered by Glattli et al. [2]. In MCBJ setups shot noise measurements where first reported by van den Brom et al. [3] revealing that the transport through single atom Au contacts is governed by a single spin degenerate transport channel. This result was extended to atomic chains by Kumar et al. [4] who also found variations in the shot noise from inelastic scattering at a vibrational mode of the chain. Subsequent to the author's report of spin polarisation in the transport channels of Co and Fe atoms on a Au(111) surface Vardimon et al. [5] found spin polarisation in the transport through NiO contacts formed using the MCBJ method.

In contrast to MCJB experiments the STM offers the ability to control with high confidence the atomic geometry of the contact formed and the involved atomic species. Consequently, shot noise measurements were performed in STM at double-barrier tunnel junctions formed by Zr-oxide islands on a Au(111) substrat [6]. With the STM tip scanning at tunnelling distances over a Au surface shot noise measurements yielded the full poissonian shot noise [7] as expected from theory. Further, Kemiktarak [8] performed shot noise measurements in the high-frequency (HF) range at tunnelling distances.

So far, shot noise measurements in STMs were restricted to large distances between the tip and sample corresponding to tunnelling barriers with low conductances. In this thesis the first successful application of the shot noise method to contacts formed in an STM are reported, where the distance between tip apex atom and adatom are near the force equilibrum distance. Thus the bonding between tip apex atom and adatom is covalent leading to conductances between $0.3\,G_0$ and $1\,G_0$ and more candidate orbitals for the formation of transport channels as compared to a tunnelling barrier. To the best of my knowledge the shot noise measurements presented in this thesis are the first to be performed at such contacts in an STM.

In order to fully understand and appreciate the presented setup and measured data a thorough comprehension of the shot noise method and the underlying transport theory is crucial. Therefore, chapter 2 introduces the reader to the model of ballistic transport through single atom contacts as well as the generation of shot noise and its interpretation. Chapter 3 describes the design of the shot noise measurement electronics that was built especially for this thesis as well as its calibration. In chapter 4 the shot noise measurements at contacts to single

Co and Fe adatoms on a Au(111) surface are presented and a discussion is given in chapter 6.

Condensed versions of the third chapter were published in:

- A. Burtzlaff, A. Weismann, M. Brandbyge, and R. Berndt, "Shot noise as a probe of spin-polarized transport through single atoms", Phys. Rev. Lett. **114**, 016602 (2015).
- A. Burtzlaff, N. L. Schneider, A. Weismann, and R. Berndt, "Shot noise from single atom contacts in a scanning tunneling microscope", Surf. Sci. **643**, 10 (2016).

2. Theory

The measurements presented in this thesis were performed using a scanning tunnelling microscope (STM). Therefore, this chapter starts with a general outline of the theoretical foundations of STM in section 2.1. Using the STM atomic geometries were formed between its tip and sample surface where the electronic transport was confined to a single atom, i.e. single atom contacts. The electronic transport through these single atoms can be described using the scattering picture of quantum ballistic transport, that is introduced in section 2.2. The shot noise generated at the atomic contacts was measured. A thorough theoretical understanding of shot noise, as provided in section 2.3.4, is crucial for comprehending the interpretation of these measurements. Since the shot noise to be measured is of the same order of magnitude as the noise of the amplifiers used in the setup, it was necessary to apply a correlation technique – the cross-spectrum method – to improve measurement precision. The cross-spectrum method, derived in section 2.5, is used to suppress the noise originating from the amplifiers from being in the same order of magnitude as the shot noise down to a neglegible fraction.

2.1. Scanning Tunneling Microscopy

In an STM a conductive tip is moved at distances of a few Ångström over a solid conductive surface to probe with potentially atomic resolution its local electronic structure and geometry. Additionally, the tip can be used to form contacts to adatoms, clusters and molecules on the surface. In contrast to e.g. the mechanically controlled break-junction method the contacts formed with an STM tip can be controlled to a high degree by thoroughly characterizing the geometric and electronic properties of the surface, the adatom and the tip before and after their formation. For a comprehensive description of the STM and STM techniques beyond the brief outline in the remainder of this subsection the reader is referred to textbooks on the subject [9].

As a basic principle the tip is brought to within a few Ångström of the conductive sample's surface and a bias voltage V_B is applied between the two. The resulting tunnelling current I is measured. The tip is attached to a piezoelectric scanner that allows it to be moved laterally over the surface with a high precision. During such a scan the z-position of the tip is usually regulated so as to keep the tunneling current constant (constant-current mode).

The tunnelling process can be described as electrons passing through a one dimensional potential barrier. Such a model explains the exponential behaviour of the tunnelling current I with the tip-sample distance. A common improved description of the tunneling process that directly links the tunneling current with the orbital structure of tip and sample is due to Bardeen [10]. By combining the states of tip and sample using first order perturbation theory the tunnelling current I at a bias voltage V and temperature T is found to depend upon the density of states (DOS) of tip (ρ_T) and sample (ρ_S) as given by [9]:

$$I(V,T) = \frac{4\pi e}{\hbar} \int_{-\infty}^{\infty} \left[f(\epsilon - eV, T) - f(\epsilon, T) \right] \rho_T(\epsilon - eV) \rho_S(\epsilon) |M|^2 d\epsilon \qquad (2.1)$$

Here f denotes the Fermi-Dirac distribution and M is the Bardeen tunneling matrix element. The latter depends on those states of tip and sample that decay into the vacuum. A common approximation of M was given by Tersoff and Hamann [11, 12] assuming an s-orbital at the tip apex. The reduction of the tip to an s-orbital is often valid since at tunnelling distances s-like states dominate the coupling to the surface.

In order to examine the sample's local density of states (LDOS) the differential conductance dI/dV is measured using a lock-in technique. Assuming a constant tip DOS the normalised quantity $\frac{dI/dV}{I/V}$ can be shown to be approximately proportional to the sample LDOS [13].

2.2. The scattering picture of quantum ballistic transport

In metals the movement of conduction band electrons constitutes an electric current. The electrons interact with their environment by scattering either at defects, other electrons or at phonons. The mean distance an electron moves between two scattering events is called the mean free path m. A region with lateral dimension l is called ballistic if l is much smaller than the mean free path

m of the conductor.

The intention of this chapter is to give an outline of quantum ballistic transport in the *scattering picture*[1], i.e. to introduce the fundamental concept of transport channels and transmission probabilities and their relation to the quantum of conductance. All derivations given are heuristic and the reader is referred to the literature [14, 15, 16, 17] for more formal and exhaustive explanations.

The scattering picture is the dominant model used to describe ballistic transport through nanostructures in general. It is based on concepts first described by Landauer [18]. His original aim was to analyse conductivity of diffusive bulk transport in a *semi-classical* way. The model has since been adopted as a versatile tool for describing and interpreting *quantum mechanical* ballistic transport through constrictions from the mesoscopic range down to single atom contacts [17]. The model will be presented here along with a set of common simple assumptions. For a more thorough overview including discussion of deviant assumptions see [15].

In order to describe the ballistic electronic transport through a single atom it is instructive to divide the system into three regions. The single atom forms a region of constriction, that is in contact with two electrodes. One of the electrodes is the surface it is lying on and the other electrode is the tip of the STM. An exhaustive description of the electronic transport through this system would require both the solution of the time dependent many body Schrödinger equation of the non-equilibrum system and a proper thermodynamic treatment of its coupling to the reservoirs. This task is very difficult and in general unsolvable.

As a remedy to this situation the many body states are replaced by a set of single-electron states in what is called the *single-electron picture*. The interpretation of these single-electron states is linked to the behaviour of discrete electrons, as will be discussed later. While this step simplifies the analysis to a copable level, it comes at a cost. Besides other many body effects both electron-electron and electron-phonon scattering are neglected as are effects relating to local charge build up, e.g. Coulomb blockade, and screening.

In the following the two electrodes that contact the ballistic transport region will be referred to as a left and a right one, without loss of generality. They are characterized to be metallic conductors with chemical potentials μ_L and μ_R and a set of single electron wavefunctions $|\psi_k^L\rangle$ and $|\psi_k^R\rangle$ each [2]. The bias voltage V

[1] It is also referred to as the Landauer model in the literature.

[2] In the literature on transport, particularly through mesoscopic systems, the electrodes are often assumed to be confined perpendicular to the current flow which leads to a discrete

being applied leads to a difference in the chemical potentials: $eV = \mu_L - \mu_R$. The process of electron transport through the constriction is described similar to the scattering of electrons at a target. The incoming wavefunctions from the left and right electrode, $|\psi_k^{L,IN}\rangle$ and $|\psi_k^{R,IN}\rangle$ are related to the outgoing wavefunctions in the left and right electrode, $|\psi_k^{L,OUT}\rangle$ and $|\psi_k^{R,OUT}\rangle$ by the scattering matrix $\mathbf{S}$:

$$\begin{pmatrix} |\psi_k^{L,OUT}\rangle \\ |\psi_k^{R,OUT}\rangle \end{pmatrix} = \mathbf{S} \begin{pmatrix} |\psi_k^{L,IN}\rangle \\ |\psi_k^{R,IN}\rangle \end{pmatrix} = \begin{pmatrix} \mathbf{r} & \mathbf{t}^\dagger \\ \mathbf{t} & \mathbf{r}^\dagger \end{pmatrix} \begin{pmatrix} |\psi_k^{L,IN}\rangle \\ |\psi_k^{R,IN}\rangle \end{pmatrix} \tag{2.2}$$

The scattering matrix consists of the transmission matrix $\mathbf{t}$, the reflection matrix $\mathbf{r}$ as well as their conjugates $\mathbf{t}^\dagger$ and $\mathbf{r}^\dagger$. For a state incident from one electrode the transmission matrix describes the resulting state in the opposite electrode. Likewise, the reflection matrix describes the part of the scattered wavefunction that is reflected back and does not cross the contact. The scattering matrix is unitary due to the conservation of charge. The matrix $\mathbf{t}^\dagger\mathbf{t}$ may be diagonalised, with a set of real eigenvalues $\tau_i \in [0, 1]$ [16]. Since the eigenstates of $\mathbf{t}^\dagger\mathbf{t}$ are orthogonal by construction they form independent[3] means for electrons to traverse the contact from one electrode to the other. Therefore they are also referred to as transport channels. A single transport channel is often compared to a single mode restricted to motion in the z-direction, that is parallel to the contact. The electron throughput in a single transmission channel is limited such that its maximum contribution to the conductance is given by the quantum of conductance[4] $G_0 = \frac{2e^2}{h} = 77.48\mu\text{S}$. The actual conductance of a transport channel is reduced by the associated eigenvalue τ. Since the transmission channels are independent the conductances of the transport channels add up to the total conductance of the contact:

$$G = \frac{2e^2}{h} \sum_i \tau_i = G_0 \sum_i \tau_i \tag{2.3}$$

The discussion so far is valid for spin degenerate transport channels. If spin degeneracy is lifted the transport channels become dependent on spin, i.e. their index is extended to include the spin state σ: $j = (i, \sigma)$. In the model these

spectrum of electronic states and a finite number of states involved in the transport process.

[3] This independence is derived within the single-electron picture. There, two or more electrons can pass the contact simultaneously in different transport channels, since Coulomb repulsion is not included.

[4] The quantum of conductance used within this thesis is the spin degenerate one.

spin transport channels j are also assumed to be independent from one another. In contrast to the spin-degenerate case a single spin transport channel can contribute at most $\frac{G_0}{2}$ to the total conductance.

At first sight it may seem peculiar for a model of *ballistic* transport to predict a *finite conductance*. In particular it leaves the question where the energy is actually dissipated, since energy dissipation is not described explicitly within the model. Indeed, from its first publication by Landauer [18] the scattering approach has undergone interpretational discussions and development, that are comprehensively reviewed in [15].

2.3. Electronic noise in single atom contacts

A measurement of the conductance can only yield information on the sum of the transmission probabilities τ_i according to equation 2.3. In this chapter it will be shown that further information on the set of τ_i is contained in the charge fluctuations or electronic noise that a contact generates. These fluctuations exist due to the quantisation of the charge being transported through the contact and the stochastic nature of the underlying transport mechanism. As a prerequisite for the discussion, the statistical quantities used to examine the fluctuations will be introduced.

2.3.1. Definition of noise quantities

For a time dependent quantity $x(t)$ let $\langle x \rangle$ denote its mean value, and $\langle (\Delta x)^2 \rangle$ its second moment or variance, where $\Delta x(t) = x(t) - \langle x \rangle$. In these definitions $\langle \cdot \rangle$ can either be the ensemble average or the time average since the process under scrutiny is assumed to be ergodic. The Fourier transform $\mathcal{F}\{x\}$ is denoted by the capital letter $X(f)$ and is defined here as:

$$X(f) = \mathcal{F}\{x(t)\} = \int_{-\infty}^{\infty} \mathrm{d}t e^{i2\pi ft} x(t) \tag{2.4}$$

The power spectral density $S_{xx}(f)$ of $x(t)$ is defined as:

$$S_{xx}(f) = 2\mathcal{F}\{\langle \Delta x(0)\Delta x(t)\rangle\} = 2\int_{-\infty}^{\infty} \mathrm{d}t e^{i2\pi ft} \langle \Delta x(0)\Delta x(t)\rangle \tag{2.5}$$

By using these definitions the variance $\langle (\Delta x)^2 \rangle$ is obtained by an integration of $S_{xx}(f)$ for positive frequencies only:

$$\langle (\Delta x)^2 \rangle = \int_0^{\infty} \mathrm{d}f S_{xx}(f) \tag{2.6}$$

In the literature on noise phenomena definitions of $\mathcal{F}\{\cdot\}$ and S_{xx} may differ from the ones used here by constant factors.

2.3.2. The importance of the external circuit

In approaching an experimental realisation of a noise measurement it is instructive to note that electronic charge fluctuations manifest themselves differently

depending on the external circuit connected to the noise source. Let R_{ext} be the external resistance that is connected in parallel to the noise source. There are two limiting cases:

- When biased at a constant current, i.e. with $R_{ext} = \infty$, the charge fluctuations lead to voltage fluctuations that can be measured across the noise source.
- When biased at a constant voltage, i.e. with $R_{ext} = 0$, the charge fluctuations lead to fluctuations in the current that flows through the noise source.

In classical electronic theory these two measurement possibilities and those with arbitrary R_{ext} are all equivalent. The current and voltage measured in a specific setup can be determined using equivalent noise sources which is a standard approach in the theory of electronic circuits, cf. [19, 20].

In the context of quantum transport this equivalence is not obvious. In theoretical descriptions of quantum transport, e.g. in the scattering picture discussed in the previous sections, a constant voltage bias is often assumed. It is modeled by a constant difference in the chemical potentials between the electrodes. For the case of a constant current bias the charge fluctuations are retained in the electrodes and lead to voltage fluctuations at the contact. This might influence the thermalisation of the electrons and the resulting fluctuations of the chemical potential difference might retroact onto the transport process. In fact, according to Blanter [16] it is not the case for the low-frequency limit. Let S be the current power spectral density in the low-frequency limit that a contact with resistance R_c generates under an ideal constant voltage bias. If this contact is connected in parallel with an external resistance R_{ext}, then the voltage and current spectral densities at the contact are given by:

$$S_{II} = \frac{S}{(1 + R_{ext}/R_c)^2} \tag{2.7}$$

$$S_{VV} = \frac{S}{(1/R_{ext} + 1/R_c)^2} \tag{2.8}$$

This result from [16] is derived within linear fluctuation theory and is also valid far from equilibrum if the conductance is replaced by the differential conductance. It is identical to the result obtained by using equivalent noise sources in the classical theory of circuits as referenced above. The validity of this simple

classical view on the measurement process beyond the low frequency limit is discussed in [21].

2.3.3. Thermal noise

In thermal equilibrum the thermal motion of the charge carriers gives rise to electronic noise. This effect was first described by Nyquist in 1928 [22] for fluctuations in electric resistors. It links the spectral voltage noise density S_{VV} and the spectral current noise density S_{II} generated by a resistor with its temperature T and with its resistance R or its conductance G, respectively:

$$S_{VV} = 4k_BTR \tag{2.9}$$

$$S_{II} = 4k_BTG \tag{2.10}$$

With k_B being the Boltzmann constant. For a formal derivation, cf. [14]. The expressions of 2.9 and 2.10 are special cases of the fluctuation-dissipation theorem. This states that "for equilibrium systems an exact relationship holds between the spectral density of fluctuations at any given frequency f, and that part of the linear response of the same system to an external perturbation of the same frequency f, which corresponds to the dissipation of the power of the perturbation"[14]. For the low frequency measurements at single atom contacts examined in this thesis the conductance G in 2.10 is replaced by the differential conductance $dI/dV(0)$ at zero bias.

$$S_{II} = 4k_BT\frac{dI}{dV}(0)$$

2.3.4. Shot noise

Out of equilibrum the charge carriers have a net mean motion that constitutes the mean current I and has the well known connection to the conductance G and applied voltage V: $I = VG$. The conductance depends on the sum of the transmission probabilities τ_i only. Therefore, it is not possible to derive information on the separate transmission probabilities from it. For information on transport properties beyond the conductance the second moment of the current turns out to be of interest. Since the electron charge is quantised the electronic noise generated by the contact represents the electron statistics of the underlying transmission process. In particular, it was found that if the transmission events

of charge carriers with charge q are uncorrelated the low-frequency component of the generated current noise spectral density S_{II} is white and depends on the mean current I as in:

$$S_{II} = 2qI \tag{2.11}$$

This relationship is called the *full shot noise* or *poissonian shot noise*. It was first derived by Schottky [23] in 1918 to describe the fluctuations occuring in a vacuum tube diode. The main prerequisite in deriving 2.11 is the lack of correlation between single charge transmission events.

Turning to a quantum mechanical description of an *electronic* transport system the main difference that has to be accounted for is the possible correlation between the charge carriers and consequently the transmission events. Reasons for these correlations comprise the full spectrum of quantum mechanical interactions, including, but not limited to, the Pauli exclusion principle and Coulomb repulsion. As an example, for a single spin polarised transmission channel Pauli repulsion prevents the electrons from passing the contact simultaneously and introduces a correlation that suppresses the noise either partially or even completely.

To elucidate this, a heuristic deduction of shot noise generated by atomic contacts at zero temperature will be given, following [14, 24] and [25]. For a thorough and formal derivation, cf. [16, 14]. The impatient reader might want to continue reading at the resulting expression 2.14.

Consider the electrons in the electrodes that approach a single transport channel at the contact to form trails of wavepackets. These wavepackets can be constructed to fullfill a couple of requirements the most important being that they are orthogonal and only contain a single electron charge each. This ensures that they obey Fermi statistics. Furthermore, the wave packets incident from the left and right electrode are assumed to be identically shaped and synchronized.

In the picture of these pulse trails the description of the transport process is reduced to the particle statistics of one state in the left and another in the right electrode, with a transmission probability τ between the two states as derived in the previous section on the scattering approach. The left and right state obey Fermi statistics $f_L(E)$ and $f_R(E)$ with chemical potentials μ_L and μ_R, respectively. They relate to the applied bias voltage V by $\mu_L - \mu_R = eV$. In the following a statistical analysis of the possible processes these pulses can undergo and their probability will be performed. From the analysis of the wavepacket's

statistics the statistics of the charge fluctuations at the contact will be infered since they are linearly related.

For the system described above there are six possible cases:

A If a wave packet arrives from each electrode both are reflected and no net current is generated. The probability for this scenario is $f_L f_R$.

B If no wave packet arrives from either electrode no current results. The probability is $p_B = (1 - f_L)(1 - f_R)$.

C An electron incident from the left is transmitted into an empty state in the right electrode with a probability $p_C = \tau f_L(1 - f_R)$. This contributes a positive pulse to the current.

D An electron incident from the right is transmitted into an empty state in the left electrode with a probability $p_D = \tau f_R(1 - f_L)$. This contributes a negative pulse to the current.

E Same as C but with the incoming electron being rejected. This does not contribute to the current.

F Same as D but with the incoming electron being rejected. This does not contribute to the current.

To perform statistics on these pulses consider the quantity n to reflect a positive pulse, a negative pulse and the absence of a pulse with $1, -1$ and 0, respectively. Its mean square deviation $\langle(\Delta n)^2\rangle = \sum_i \frac{1}{N}(n_i - \langle n\rangle)^2$ can be calculated by weighing the contributions from each of the cases above with its respective probability. The contributions are $(1 - \langle n\rangle)^2$ for the case of an electron being transmitted from left to right (C), $(1 + \langle n\rangle)^2$ for the case of an electron being transmitted from right to left and $\langle n\rangle^2$ for all other cases that don't result in a pulse transfer. In total this yields:

$$\begin{aligned}\langle(\Delta n)^2\rangle &= (1 - \langle n\rangle)^2 p_C + (1 + \langle n\rangle)^2 p_D + \langle n\rangle^2 (1 - p_C - p_D) \\ &= p_C + p_D - 2\langle n\rangle(p_C - p_D) + \langle n\rangle^2 \\ &= p_C + p_D - (p_C - p_D)^2\end{aligned}$$

In the last step the insight is used that $(p_C - p_D)$ is actually $\langle n\rangle$. To form a relation with the variance of the current $\langle i^2\rangle$ that flows through the contact, the

probabilities p_C and p_D are replaced by their specific values, the linear dependence of the current on the particle statistics is accounted for by the constant L. Finally, the non-constant energy dependence of the expression is taken into account by an energy integration:

$$\begin{aligned}\langle i^2\rangle = L\int_{-\infty}^{\infty} dE\,\tau(E)\left[f_L(E)[1-f_R(E)]+f_R(E)[1-f_L(E)]\right]\\ -\tau^2(E)\left[f_L(E)-f_R(E)\right]^2\end{aligned}$$

Since contributions from independent conductance channels simply add, the extension from the single channel case discussed so far to multiple channels is straightforward:

$$\begin{aligned}\langle i^2\rangle = L\int_{-\infty}^{\infty} dE\sum_i\{\tau_i(E)\left[f_L(E)[1-f_R(E)]+f_R(E)[1-f_L(E)]\right]\\ -\tau_i^2(E)\left[f_L(E)-f_R(E)\right]^2\end{aligned} \tag{2.12}$$

Next, the transition to the spectral current density S_{II} needs to be performed. In particular, we are interested in its low frequency component $S_{II}(f\to 0,V)$. Low frequency refers to the case where the time scale of individual electrons passing through the contact is small compared with the spectral time scale $1/f$. Consider the Fourier transform of the current:

$$S_{II}(f\to 0,V) = 2\left|\int_{-\infty}^{\infty}\mathrm{d}t e^{i2\pi ft}\langle i(t)\rangle\right|^2 \tag{2.13}$$

The variation of $e^{-i2\pi ft}$ with t is much slower than the variation of $i(t)$. Therefore the latter can replaced by its average and the relation between $S_{II}(f\to 0,V)$ and $\langle i^2\rangle$ becomes linear: $S_{II}(f\to 0,V) = M\langle i^2\rangle$. For a discussion of this argument see [25]. For formal derivations the reader is referred to the literature [14].

To determine the constant $K := ML$ consider the zero bias case $V = 0$. There, the current noise density has to reduce to the thermal noise of equation 2.10. First, since $f_L = f_R = f$ for zero bias equation 2.12 reduces to:

$$S_{II}(f\to 0,V=0) = K\int_{-\infty}^{\infty} dE\,2f(E)(1-f(E))\sum_i\tau_i(E)$$

Using $f(E)(1-f(E)) = -k_BT\frac{\partial f}{\partial E}$ and equation 2.3 this yields:

$$\begin{aligned} S_{II}(f \to 0, V = 0) &= -2Kk_BT \int_{-\infty}^{\infty} dE\, \frac{\partial f}{\partial E} \sum_i \tau_i(E) \\ &= 2Kk_BT \frac{\pi\hbar}{e^2} \frac{e^2}{\pi\hbar} \int_{-\infty}^{\infty} dE\, (-\frac{\partial f}{\partial E}) \sum_i \tau_i(E) \\ &= 2Kk_BT \frac{\pi\hbar}{e^2} G \\ \Rightarrow 4k_BTG &= 2Kk_BT \frac{\pi\hbar}{e^2} G \\ \Rightarrow K &= 2\frac{e^2}{\pi\hbar} \end{aligned}$$

Consider the zero temperature case and without loss of generality $\mu_L > \mu_R$. Taking into account that $f_L(E) - f_R(E) \in [1, 0]$ for zero temperature it follows $(f_L(E) - f_R(E))^2 = f_L(E) - f_R(E)$. Then equation 2.12 reduces to:

$$\begin{aligned} S_{II} &= 2\frac{e^2}{\pi\hbar} \sum_i \tau_i(\mu_L - \mu_R) - \tau_i^2(\mu_L - \mu_R) \\ &= 2eV \frac{e^2}{\pi\hbar} \sum_i \tau_i(1 - \tau_i) \\ &= 2eVG_0 \sum_i \tau_i \frac{\sum_i \tau_i(1-\tau_i)}{\sum_i \tau_i} \\ S_{II} &= 2eI \frac{\sum_i \tau_i(1-\tau_i)}{\sum_i \tau_i} =: 2eIF \end{aligned} \tag{2.14}$$

This main result shows that the low-frequency component of the current noise is proportional to the mean current I and the so called Fano factor F. The latter thus constitutes the ratio between the full shot noise $2eI$ and the result obtained for the particular quantum mechanical system and is in the interval $[0, 1]$ within the applied model. It links the transmission probabilities τ_i of the eigenchannels with the increase of the generated shot noise with the mean current I. While it is not a one-to-one relationship, the combination of Fano factor and conductance can yield valuable information on the number of transmission channels, in some cases the transmission probabilities themselves, and even the spin-polarisation.

To elucidate the interplay of conductance, Fano factor and transmission probabilities consider the case of a single conduction channel with a transmission probability τ. The contribution of this channel to the total Fano factor is given by the numerator in 2.14: $\tau(1-\tau)$. This expression has two extremal cases.

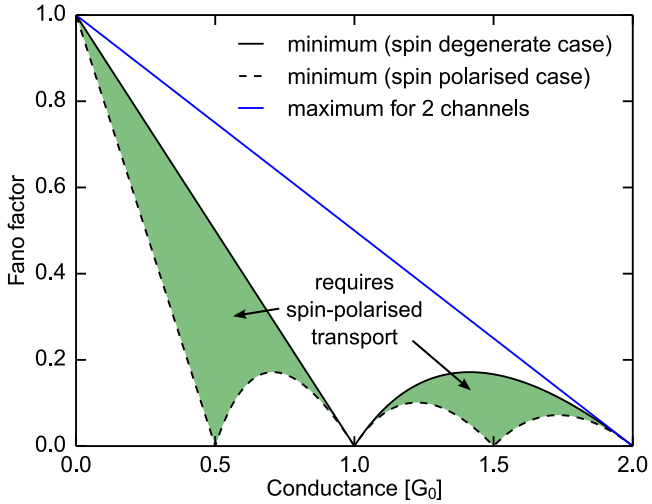

Figure 2.1.: Fano factor vs. conductance diagram. If a conductance G is constructed from fully transparent channels, fully closed channels and only one single partially transmissive spin-degenerate channel the corresponding Fano factor will lie on the black line. This constitutes the minimum Fano factor possible for spin-degenerate channels. If spin-degeneracy is lifted the green areas become accessible.

First, the contribution of a single channel reaches its maximum $\frac{1}{4}$ for $\tau = \frac{1}{2}$. Consequently, the maximum Fano factor for n channels is reached if $\tau_i = 0.5$ for all channels i. In figure 2.1 the maximum Fano factor for a total of 1 and 2 channels are displayed. Second, for $\tau = 0$ or $\tau = 1$ the contribution of the channel to the Fano factor vanishes completely. Thus, the transport through a fully open channel does not contribute to the noise. Therefore, for a given conductance G the minimum factor possible is reached with a set of τ_i such that $G = G_0 \sum_i \tau_i$ and all but one differs from 0 and 1: $0 \leq \tau_0 \leq 1$ and $\tau_i = 0$ or $\tau_i = 1$ for $i > 0$. In figure 2.1 the dependence of this minimum Fano factor with the contact conductance is displayed as a black curve. In particular, for conductances that are integer multiples of G_0 a Fano factor of zero is possible, if the transport is formed by fully conducting channels only. In those cases the noise is completely suppressed.

So far, the eigenchannels where taken to be spin degenerate. If the spin degeneracy is lifted each spin channel can only contribute $\frac{G_0}{2}$ to the overall conductance yet its contribution to the Fano factor remains unchanged. This has consequences for the minimum Fano factor discussed in the previous paragraph. Its dependence on the contact conductance for the spin-polarised case is displayed in 2.1 as

a black dashed line. While the Fano factor is 1 in the limit $G \to 0$ as for the non-spinpolarised case, it decreases linearly and reaches 0 at $0.5\,G_0$. This leads to the existence of the green hatched region in figure 2.1 between the minimum Fano factor for spin degenerate and for spin polarised transport that are forbidden for spin degenerate transport within this model. Measurements of conductance and Fano factor that lie in these regions therefore indicate spin polarised transport.

The preceding discussion was performed for the zero temperature case. For non-zero temperature the current noise power density S_{II} at zero bias needs to be the thermal noise density $4k_BT$ discussed earlier. One might expect a simple addition of equations 2.10 and 2.14. In fact, the contributions of these two noise sources are intertwined with each other and do not simply add. The expression for the total noise for non-zero temperature agreed upon in the literature is attributed to Lesovik [26] and cited here from [16]:

$$S_{II}(V) = 2eVG_0 \coth\left(\frac{eV}{2k_BT}\right) \sum_n \tau_n(1-\tau_n) + 4k_BTG_0 \sum_n \tau_n^2 \qquad (2.15)$$

Figure 2.2 displays this expression for different temperatures. For the limit $T \to 0$ it reduces to the linear dependence $S_{II} = 2eGVF = 2eIF$ of expression 2.14 as expected. At non-zero temperature and zero bias the thermal noise density is recovered. For high bias voltages $eV \gg 2k_BT$ it becomes asymptotically linear with a slope of $2eGF$, independent of the temperature.

The expression 2.15 can be rearranged[5] to depend on the full shot noise density $S_0 = 2eI$, the thermal current noise density $S_\theta = 4k_BTG$ and the Fano factor F:

$$\begin{aligned} S_{II}(V) &= 2eVG_0 \sum_n \tau_n \coth\left(\frac{2eVG}{4k_BTG}\right) \frac{\sum_n \tau_n(1-\tau_n)}{\sum_n \tau_n} + 4k_BTG_0 \sum_n \tau_n^2 \\ &= 2eI \coth\left(\frac{S_0}{S_\theta}\right) F + 4k_BTG_0(1-F) \sum_n \tau_n \\ &= S_0 \coth\left(\frac{S_0}{S_\theta}\right) F + S_\theta(1-F) \end{aligned} \qquad (2.16)$$

In the first step it was used that $F = 1 - \frac{\sum_n \tau_n^2}{\sum_n \tau_n} \quad \leftrightarrow \quad \sum_n \tau_n^2 = (1-F)\sum_n \tau_n$. In contrast to the original equation 2.15 in the new one 2.16 the Fano factor F replaces the explicit dependence on the transmission coefficients. This makes it a more versatile choice in fitting the experimental data.

[5] Alexander Weismann, private communication

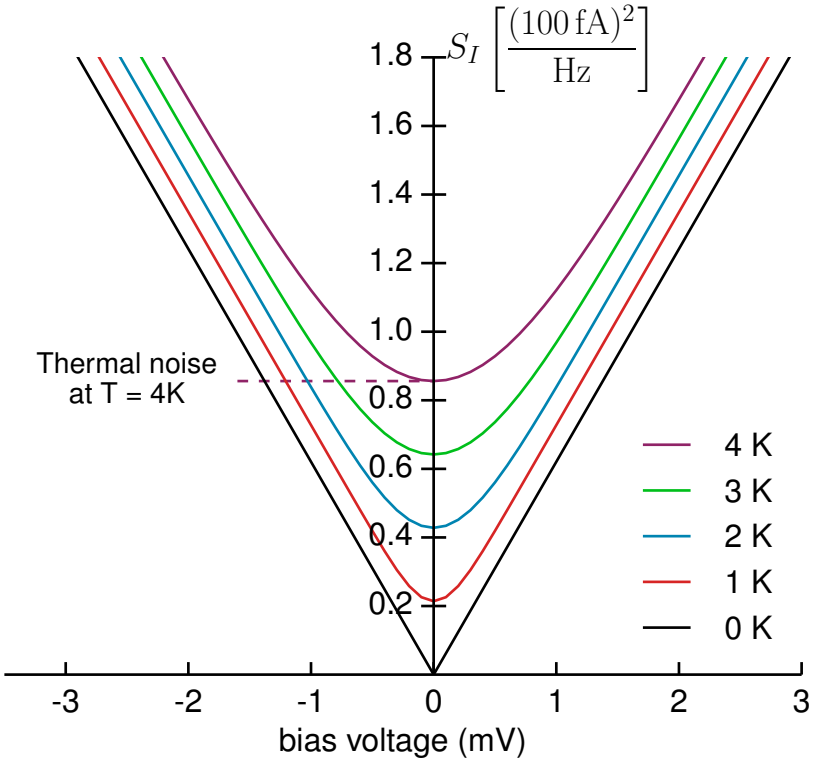

Figure 2.2.: The dependence of the current noise density on the applied bias voltage for different temperatures according to Lesovik's expression (2.15). For zero temperature the dependence is linear with a slope of $2eGF$. For non-zero temperature at zero bias the noise density is entirely thermal in nature, while at higher bias the dependence becomes asymptotically linear again with a slope of $2eGF$.

2.4. Relation between quantum model and measurement

> *None of the cited theory papers make an attempt to relate in detail to the actual noise measurement. They simply invoke operators, with varying degrees of justification. We will not do all that much better, but will try to introduce a little physics.*
>
> — R. Landauer and Th. Martin, Physica B 175 (1991), 167–177

Within the theoretical model developed in the preceding section shot noise is completely suppressed for a single fully-transparent transport channel. The charge transmission events thus occur in fully correlated way, i.e. at constant time intervals. In a publication by Thibault et al. [27] this correlation has been measured directly. The electronic noise at frequencies up to 13 GHz generated by a bulk Al/Al oxide/Al tunnel junction at a base temperature of 8 mK were measured. Using a correlation measurement technique the authors found that the electrons pass the contact at a regular "pace of one electron per channel per spin direction every $\frac{h}{eV}$"[27]. They interpret their findings as a consequence of both Pauli-repulsion and the Heisenberg uncertainty relation.

The electronic charge fluctuations generated by the shot noise is also associated with the emission of light from the contact. The dependence of the light intensity and wavelength on bias voltage and contact conductance is associated with single and multi electron processes in the electrodes generating plasmons that emit light during their decay. Under adequate circumstances the dependence of the light intensity emitted by a Ag-Ag(111) contact on the tip-sample distance – and thus on the conductance – can be associated with the minimum Fano factor line in 2.1 [28]. For an overview on light emission at atomic contacts the reader is referred to [29].

2.5. Cross correlation measurements

Both the thermal noise density of the atomic contact and the increase of the noise density due to the shot noise are of the same order of magnitude as the two amplifier's equivalent input voltage noise density ($2.2\,\mathrm{nV}/\sqrt{\mathrm{Hz}}$). In order to separate the noise density originating from the atomic contact from the amplifier's noise contributions, the *cross spectrum* method is applied. It will be explained in this section following [30].

The main idea of this method is to measure a voltage signal $c(t)$ using two amplifiers simultaneously as depicted in figure 2.3. Each of the two amplifiers adds its own internal voltage noise $a(t)$ and $b(t)$ to the signal and finally amplifies the sum by its gain G:

$$x(t) = G(c(t) + a(t)) \tag{2.17}$$

$$y(t) = G(c(t) + b(t)) \tag{2.18}$$

Since $a(t)$ and $b(t)$ originate from two spatially separated circuits they are uncorrelated. In contrast, the signal $c(t)$ is correlated in $x(t)$ and $y(t)$. By looking at the correlation between $x(t)$ and $y(t)$ the spectral density S_{cc} of $c(t)$ can be recovered, as shown in the following paragraphs.

Before explaining the use of this correlation it is necessary to define a set of quantities. In the following, $G = 1$ is assumed without loss of generality. The time signal $c(t)$ is stationary and ergodic and its Fourier transform[6] $\mathcal{F}\{c(t)\}$ is denoted by the capital letter $C(f)$. In any experiment time signals can only be acquired for a finite measurement time T. The truncated signal and its Fourier transform are denoted $c_T(t)$ and $C_T(f)$ respectively. Likewise the expectation value $\mathbb{E}\{\cdot\}$ of any statistical quantity can only be approximated by the average $\langle\cdot\rangle_m$ over a finite number m of realisation.

The quantity of interest from signal c is its power spectral density (PSD), defined by:

$$S_{cc}(f) = 2\mathcal{F}\{R_{cc}(t')\} \tag{2.19}$$

and R_{cc} is the autocorrelation function of the time series $c(t)$:

$$R_{cc}(t') = \mathbb{E}\{c(t)c(t+t')\} \tag{2.20}$$

[6] Throughout the thesis power spectral densities S are defined such that the normalisation $\sqrt{1/T \int dt s(t)^2 dt} = \int_0^\infty |S(f)|^2 df$ holds. The spectral power is thus contained in the positive part of the spectrum. This explains the factor 2 in the definition of S_{cc}.

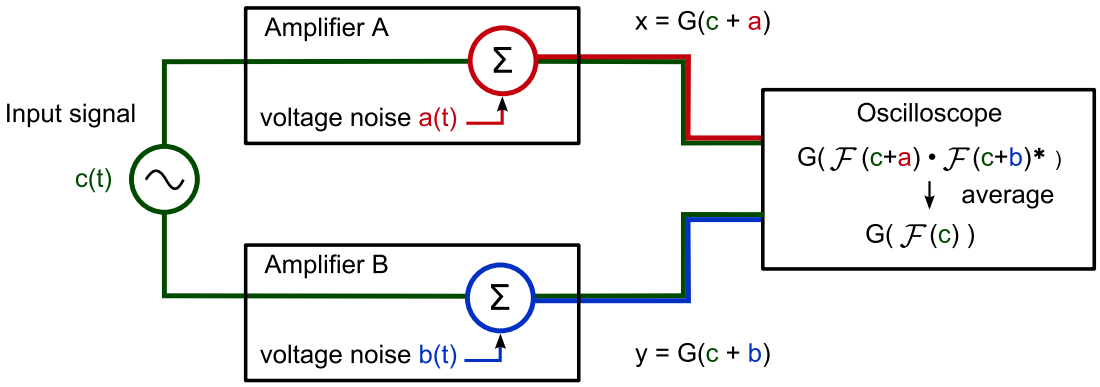

Figure 2.3.: Setup of a cross spectrum measurement. The target voltage signal $c(t)$ is amplified by a factor G using two amplifiers A and B in parallel. Their output voltage is acquired by an oscilloscope. Each of the two amplifiers adds a voltage noise $a(t)$ and $b(t)$ to the target signal. These noise signals are uncorrelated since they are generated inside the spatially separated amplifiers. By calculating the cross power spectral density of the two signals $x(t)$ and $y(t)$ as described in the text, the power spectral density of the target signal $c(t)$ can be recovered.

Since the process is ergodic and stationary the Wiener-Khintchine theorem is applicable and provides a means to calculate the PSD using the Fourier transform rather than the time signal:

$$\mathbb{E}\left\{S_{cc}(f)\right\} = \mathbb{E}\left\{\lim_{T\to\infty}\left[\frac{1}{T}C_T(f)C_T^*(f)\right]\right\} \tag{2.21}$$

In order to be applied to a real world measurement the expectation value is replaced with the average over m measurements as described above:

$$\langle S_{cc}(f)\rangle_m = \frac{1}{T}\langle C_T(f)C_T^*(f)\rangle_m \tag{2.22}$$

For two signals $x(t)$ and $y(t)$ the following quantities can be defined in analogy to the definitions of $S_{cc}(f)$, $\mathbb{E}\left\{S_{cc}(f)\right\}$ and $\langle S_{cc}(f)\rangle_m$.

$$S_{xy}(f) = 2\mathcal{F}\left\{R_{xy}\right\} \tag{2.23}$$

$$\mathbb{E}\left\{S_{xy}(f)\right\} = \mathbb{E}\left\{\lim_{T\to\infty}\left[\frac{1}{T}X_T(f)Y_T^*(f)\right]\right\} \tag{2.24}$$

$$\langle S_{xy}(f)\rangle_m = \frac{1}{T}\langle X_T(f)Y_T^*(f)\rangle_m \tag{2.25}$$

$S_{xy}(f)$ is called the *cross power spectral density* or *cross spectrum* of x and y.

The use of the cross spectrum becomes obvious when equation 2.24 is expanded with equations 2.17 and 2.18, leaving out the frequency dependence for clarity:

$$\begin{aligned}
\mathbb{E}\{S_{xy}\} &= \frac{1}{T}\mathbb{E}\{X_T Y_T^*\} && (2.26)\\
&= \frac{1}{T}\mathbb{E}\{[C_T + A_T]\cdot[C_T + B_T]^*\} && (2.27)\\
&= \frac{1}{T}[\mathbb{E}\{C_T C_T^*\} + \underbrace{\mathbb{E}\{C_T B_T^*\}}_{=0} + \underbrace{\mathbb{E}\{A_T C_T^*\}}_{=0} + \underbrace{\mathbb{E}\{A_T B_T^*\}}_{=0}] && (2.28)\\
&= S_{cc} && (2.29)
\end{aligned}$$

Because $a(t)$,$b(t)$ and $c(t)$ are assumed to be uncorrelated the expectation values of CB^*, AC^* and AB^* vanish. The expectation value of the cross spectral density is thus identical to the power spectral density of the correlated part of $x(t)$ and $y(t)$ regardless of the added uncorrelated contributions.

For the case of a finite number m of realisations the average $\langle S_{xy}(f)\rangle_m$ is found to converge towards the expectation value S_{cc}, in full analogy to the expectation value $\mathbb{E}\{S_{xy}\}$:

$$\begin{aligned}
\langle S_{xy}(f)\rangle_m &= \frac{1}{T}\langle X_T Y_T^*\rangle_m && (2.30)\\
&= \frac{1}{T}\langle[C_T + A_T]\cdots[C_T + B_T]^*\rangle_m && (2.31)\\
&= \frac{1}{T}[\langle C_T C_T^*\rangle_m + \langle C_T B_T^*\rangle_m + \langle A_T C_T^*\rangle_m + \langle A_T B_T^*\rangle_m] && (2.32)\\
&= S_{cc} + \mathcal{O}(\sqrt{1/m}) && (2.33)
\end{aligned}$$

Here the Landau notation $\mathcal{O}$ is used to describe the convergence behaviour. The convergence behaviour follows a $\sqrt{1/m}$-law for the asymptotic case $|S_{xy}| \gg S_{cc}$ but it is hard to assess theoretically for $|S_{xy}| \approx S_{cc}$. Therefore, for the data analysis performed in this thesis a quantitative theoretical assessment of the convergence is unreasonable. Instead, the convergence is analysed by looking at the Fano factor determined from cross spectra with an increasing number of averages, see section 3.3.5.

In the remainder of this thesis both $\mathbb{E}\{S_{xy}(f)\}$ and the experimentally accessible $\langle S_{xy}(f)\rangle_m$ will be referred to as cross (power) spectral density or simply cross spectrum S_{xy} since they are easily discernable from the context.

3. Measurement process

3.1. Introduction

Turning to the experimental realisation a noise measurement setup was built that extends an STM operating under ultra-high vacuum (UHV) conditions and at liquid helium temperature. Since fine-grained control on the electronics and non-standard approaches are pivotal for successfully performing the electronic noise measurements, a large proportion of the instruments used in the measurement setup were specially designed and home-built by the author[1].

The chapter is divided into two parts. In the first part the measurement setup is described. It starts with a simplified, methodical overview (3.2.1) and a summary (3.2.2) on the fundamental considerations that lead to the final design, and the limitations they entail. Following that, the different parts and aspects of the setup are described in more technical detail. The second part of this chapter concerns the data analysis and the calibration of the measured quantities.

3.2. Measurement setup

3.2.1. Overview

For ease of readability a simplified description of the measurement setup is given in the following paragraph. It is depicted in figure 3.1. Atomic contacts were formed in a low temperature STM that is located at the bottom of a He-bath-cryostat. Two stainless steel wires $\approx 1.3\,\mathrm{m}$ in length connect the two leads of the contact to the feedthroughs at the upper part of the cryostat. Outside the cryostat these two signals are connected using low-noise coaxial cables of minimal length to an shielded box containing the complete first stage of the measurement electronics. The first subcircuit in this box – the switching subcircuit (see section 3.2.5) – enables the signals to be remotely switched between the STM

[1] with considerable and invaluable help and consultation by Hans-Joachim Neumann

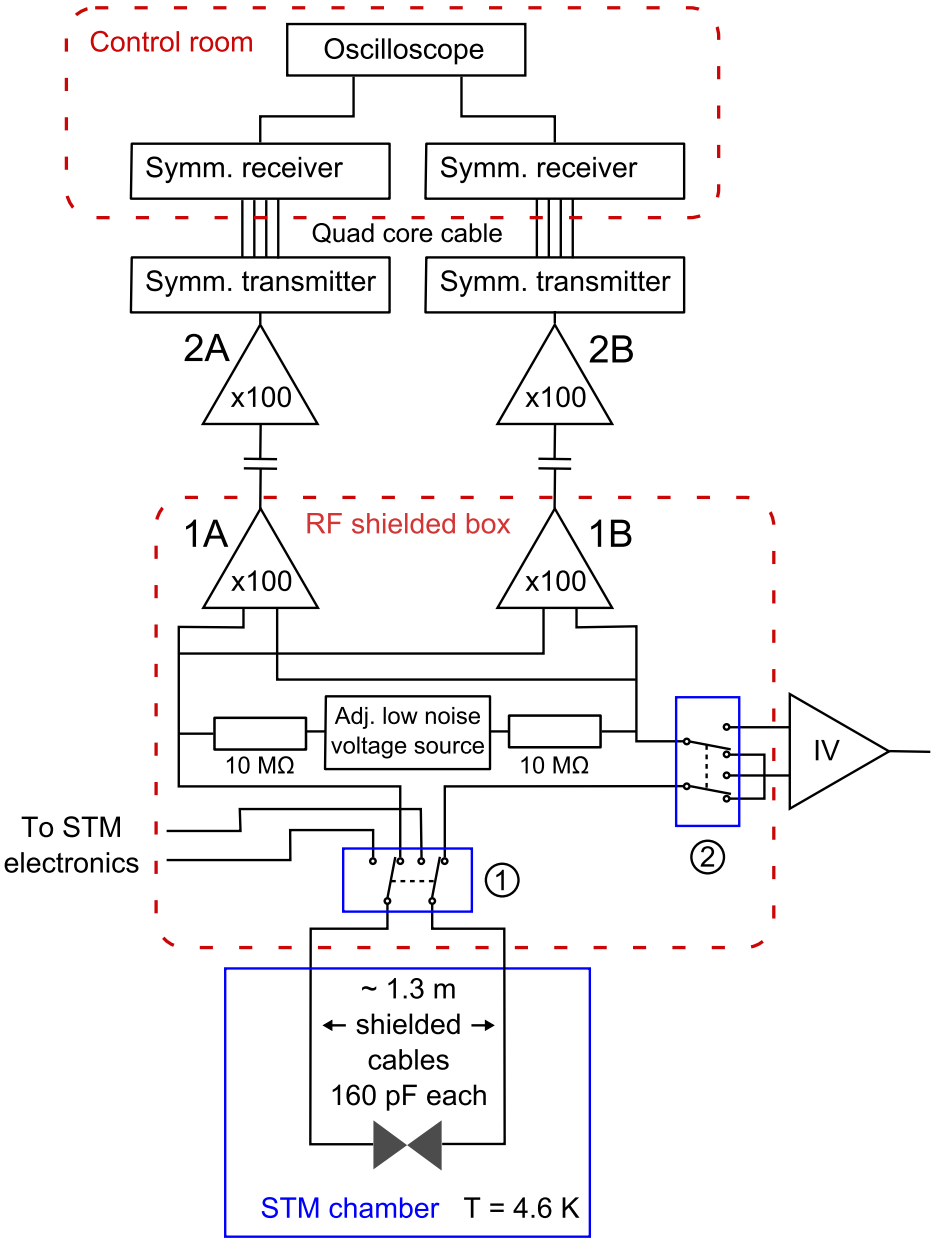

Figure 3.1.: Simplified schematic of the measurement setup. Tip and sample of the low temperature STM are each connected to relay (1) via shielded stainless steel cables. These can be switched between the STM electronics and the noise measurement setup using relay (1). In the latter state the contact is biased by a remotely adjustable constant current generated by a voltage source in series with 20 MΩ. The voltage fluctuations at the contact are measured using the two home built amplifiers (1A) and (1B). Using relay (2) a Femto DLPCA-200 IV-converter can be switched into the circuit to measure the biasing current flowing through the contact. The AC-coupled output signals of amplifiers 1A and 1B are further amplified before being transmitted to the oscilloscope in the control room using a custom built symmetric transmission line. For a detailed description see section 3.2.1.

electronics and a dedicated noise measurement setup. For scanning and contact formation the two cables can be connected to the bias and tunnelling current connections of the standard STM control electronics using relay 1 (figure 3.1). After a contact has been constructed in this mode, relay 1 is switched such that the the two wires are connected to the home-built noise measurement setup. In the noise measurement setup an atomic contact can be biased by a home-built battery powered ultra-low noise constant current source (see section 3.2.7) that is remotely adjustable. To measure the current passing through the contact a Femto DLPCA-200 IV-converter can be switched into the circuit using relay 2. The voltage fluctuations that the contact generates are measured differentially and amplified by a factor of 100 by two home-built amplifiers 1A and 1B in parallel. The output signals of amplifiers 1A and 1B leave the shielded box and form the inputs for the Stanford Research SR560 voltage amplifiers 2A and 2B, respectively. Each of the aforementioned connections is AC-coupled using a 1 nF capacitor. The latter amplifiers are set to a gain of 100 and thus the overall voltage gain of the signal chain is 10000. The output signals from amplifiers 2A and 2B are transmitted approximately 7 m from the laboratory to the control room using two home-built symmetric transmission lines[2]. Finally, the two signals are sampled using an Agilent DSO-90254A digital storage oscilloscope. For each constant current bias generated by the adjustable current source the cross spectrum of the acquired amplified voltage signals from the two amplifications chains is calculated and averaged yielding the noise power density spectrum of the voltage flucutations at the contact. For ease of readability the preceding description of the measurement setup has been simplified. Details that are not essential to the understanding of the measurement process but pivotal for successfully performing the measurement have been left out. In the following subsections different parts of the setup will be described in detail to shed light onto particular design considerations.

3.2.2. General measurement considerations

The charge fluctuations constituting the electronic noise of an atomic contact can be measured either as voltage noise or as current noise depending on the external circuit used for biasing, as described in section 2.3.2. Building on the works of Glattli [2] and van den Brom [3] a differential measurement of the voltage fluc-

[2]The two symmetric transmission lines were custom designed and built for the noise measurement by Hans-Joachim Neumann.

tuations from the atomic contact biased at a constant current was choosen. The main advantages of this choice are fourfold. First, using a differential measurement a high immunity to electronic interference noise can be achieved. Second, voltage amplifiers do not induce additional current dependent noise into the measurement circuit. In contrast, the commonly used operational amplifier circuit for current to voltage conversion generates shot noise itself and feeds it into the measurement circuit. Third, since two voltage amplifiers in parallel do not significantly interfere with each other, the cross-spectrum (see section 2.5) method can be applied to suppress their input voltage noise and enable voltage measurements below the input voltage noise of the amplifiers. Fourth, an adjustable constant current source needed to bias the contact is easier to build in such a way that it does not add current dependent noise into the circuit (see section 3.2.7) compared to an adjustable constant voltage sources with the same property.

Measuring the charge fluctuations in a voltage measurement setup entails one major drawback: The source resistance forms a low pass filter with the capacitance towards ground of the wires connecting to it (see fig. 3.2). The source resistance is given by the atomic contact to be measured and is of the order of $1G_0$ The capacitance consists of the capacitance of the cables center conductor towards ground – the cable capacitance – as well as the input capacitance of the amplifiers. The low pass filter characteristic thus limits the noise signal to bandwidths around $f_{-3\mathrm{dB}} \approx \frac{G_0}{\pi C_{\mathrm{cable}}} \approx 100\,\mathrm{kHz}$ and yields an *upper limit* to the frequency interval in which the noise spectra can be evaluated. Great care had to be taken not to decrease this frequency interval further, in particular by not adding any unavoidable capacitances to the two signal lines.

In the low frequency part of the noise spectrum however a noise with a 1/f-like spectrum emerges from the biased contact. The corner frequency, i.e. the frequency at which the low frequency noise becomes neglegible compared to the shot noise to be measured increases with the applied current. It thus poses a *lower limit* to the frequency interval in which the noise spectra can be evaluated.

In order for the cross correlation method described in section 2.5 to be maximally effective in suppressing any noise not originating from the contact a four point measurement would be needed. Yet two cables connecting each side of the contact with the feedthroughs instead of one would also double the cable capacitance. Since this in turn would reduce the already tight bandwidth of the noise signal by a factor of 2, a two point measurement was chosen. The main drawback of this choice is, that the signal also contains thermal noise of the stainless steel

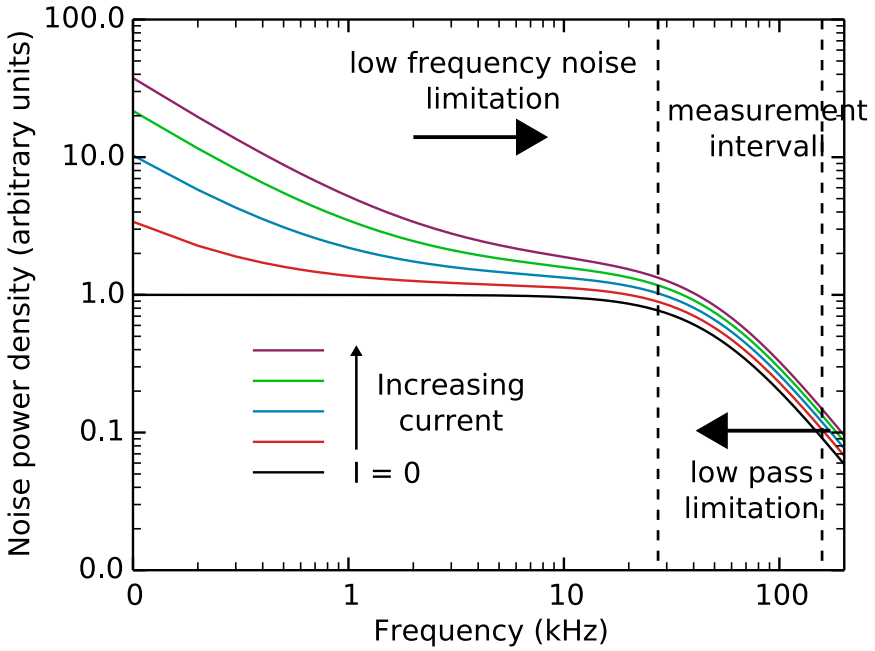

Figure 3.2.: Qualitative illustration of the restrictions on the frequency interval suitable for evaluating the shot noise. Black curve represent the zero bias spectrum. At low frequencies the noise spectra for non-zero bias are dominated by $1/f$-like noise that increases with the applied bias current. The low pass characteristic induced by the cable capacitance forms an upper limit to the available bandwidth. In the frequency interval between these two limits a homogeneous increase of the noise power density due to shot noise can be observed.

cables that connect both tip and sample with the feedthroughs at the top of the cryostat. This is easily accounted for in the data analysis.

3.2.3. Electronic considerations on the noise measurements

Concerning the measurement electronics there are two pivotal criteria the design has to fulfill:

1. (**Symmetry**) The transmission characteristics of the signal lines that connect the contact with the amplifiers have to be as similar as possible. This mainly concerns the capacitive property of the wires.

2. (**Minimal capacitance**) The capacitance towards ground of the two signal lines needs to be minimized since it determines the bandwidth of the noise spectrum.

The second fundamental design goal has been explained in the previous section.

To understand the first one consider the differential voltage measurement setup depicted in figure 3.3. The time signal $V(t)$ generated by a source with internal resistance R_C is measured by a differential voltage amplifier. The two leads connecting the source to the amplifier have capacitances C_A and C_B towards common ground. Additionally a voltage $V_{\mathrm{CM}}(t)$ can be induced.

First, consider the case $C_A = C_B$ with the voltage source V_{CM} disconnected. Then both V and R_{C} can be split in half and the setup is symmetric with respect to the blue dashed symmetry line. The two signal paths above and below the symmetry line both form equal low pass transfer characteristics lp from $\frac{R_{\mathrm{C}}}{2}$ and $C_{\mathrm{A/B}}$. The ideal differential amplifier amplifies the difference $V_+ - V_-$ which in this case is $lp(V)$. If a common mode signal V_{CM} is induced, it will undergo the same two transfer characteristics such that the input at the amplifiers are: $V_\pm = lp(V_{\mathrm{CM}} \pm \frac{V}{2}) = lp(V_{\mathrm{CM}}) \pm lp(\frac{V}{2})$. At the amplifier the common mode signal cancels out

$$V_+ - V_- \quad = lp(V_{\mathrm{CM}}) + lp(\tfrac{V}{2}) - (lp(V_{\mathrm{CM}}) - lp(\tfrac{V}{2})) = lp(V)$$

Next, consider the case $C_A \neq C_B$ with V_{CM} disconnected. The symmetry is broken and signals above and below the blue dashed line transfer according to different transfer characteristics lp_A and lp_B, respectively. The difference $V_+ - V-$ of the amplifier inputs is not $lp(V)$ but $V(t)$ transformed according to a distorted transfer characteristic *dist* that depends on C_A and C_B. This particular aspect does not generally prohibit a precise measurement of V, since the transfer characteristic is constant and can be calibrated (see section 3.3.2). Yet a common mode signal V_{CM} will also undergo two different characteristics

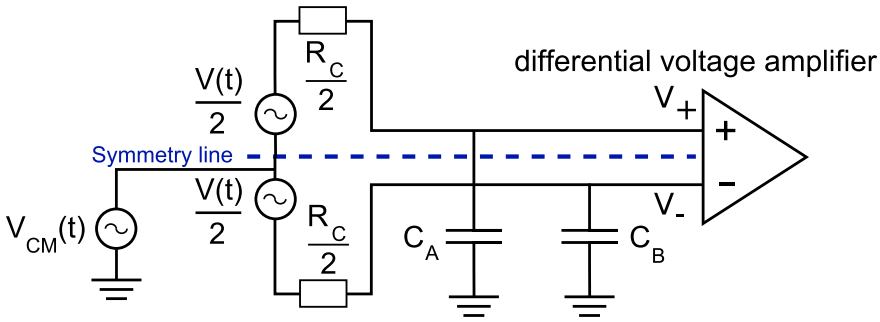

Figure 3.3.: Schematic of the voltage noise $V(t)$ generated by a contact with resistance R_C being measured by a differential voltage amplifier. The two cables connecting the contact to the amplifier have capacitances C_A and C_B towards ground. In conjunction with the contact resistance ($\frac{R_C}{2}$) each of them forms a low pass filters. In the ideal case $C_A = C_B$ the setup is symmetric with respect to the blue symmetry line. For a discussion of the the symmetric as well as the debalanced ($C_A \neq C_B$) case see text.

such that at the amplifier input

$$V_+ - V_- \quad = lp_A(V_{\mathrm{CM}}) - lp_B(V_{\mathrm{CM}}) + dist(V)$$

Since lp_A and lp_B are not identical V_{CM} will not be completely suppressed as in the symmetric case.

Figure 3.4 shows a detailed representation of the electronic circuit from the atomic contact inside the STM to the inputs of the amplifiers. Tip and sample forming the atomic contact are connected with 1.3 m shielded stainless-steel cable to the shielded box containing the amplifiers. The cables have a resistance R_{cable} =159 Ω and a capacitance of ≈160 pF. Inside the shielded box the cable connect to two home-built amplifiers 1A and 1B. Their inputs are characterised by an input resistance R_{amp} and an input capacitance C_{amp}. Furthermore the wires connect to the adjustable voltage source outputs $V_{\mathrm{vs},1}$ and $V_{\mathrm{vs},1}$ via two resistors with a resistance of $\frac{R_S}{2}$ =10 MΩ at each of the outputs. Thereby the impact of capacitance C_{VS} ≈290 pF of the voltage source towards ground on the transfer characteristics of the upper and lower signal path is minimized (see also section 3.2.7). C^A_{tot} and C^B_{tot} are effective capacitances representing the cable capacitances as well as parasitic capacitances of the wires inside the shielded box. A symmetry of the effective electronic characteristics above and below the blue symmetry axis is desirable as explained in the previous paragraph. To achieve this the variable capacitance C_V was adjusted so that the total capacitance towards ground measured at the upper and lower signal path match. The

capacitance was measured using a multimeter. Since the cable resistance R_C keeps the upper and lower signal lines from being purely capacitive an absolute capacitance measurement will yield different results depending on the measurement method and not be meaningful in itself. A matching of the measured capacitances however entails the desired matching of the transfer characteristics.

3.2.4. Connections inside the cryostat

To ensure a minimal magnetic coupling of electromagnetic interferences into the measurement circuit the two stainless-steel cables were placed adjacent to each other and loosely twisted multiple times at distances around 5–10 cm. This reduces the area between the two cables and thereby the inductive coupling of electromagnetic interference signals into the signal path. The twisting of the cables minimized that type of coupling even further since inductive signals induced in two adjacent "eyes" of the cable cancel each other to a high degree. The symmetry criteria described in the previous subsection is met by adding an adjustable capacitance to the wire with the slightly lower capacitance. Before each measurement session this adjustable capacitance is tuned so as to match the total effective capacitances of the two wires.

3.2.5. The switching subcircuit

The task of the switching subcircuit is to switch the two wires connected to the contact between the STM electronics and the dedicated noise measurement setup. Additionally, an I/V converter can be inserted into the circuit in noise measurement mode, to measure the current flowing through the contact. Development and testing of the setup revealed several additional considerations that were crucial for successfully performing the noise measurements. First, the switching of any relay in the switching subcircuit (the relays 1 and 2 in figure 3.1) generates an audible clicking sound. Undamped, this sound impulse can propagate through the cryostat down to the contact and alter it. As a remedy the circuit board of the switching subcircuit was attached to the metal casing using rubber damping and the upper part of the cryostat was acoustically damped using special sound damping foam and thick blankets. Second, the switching of the relays generates voltage pulses that are able to alter and destroy the contact. As a countermeasure it has proven successful to first short circuit the two leads coming from the contact using a single relay before switching any other relay.

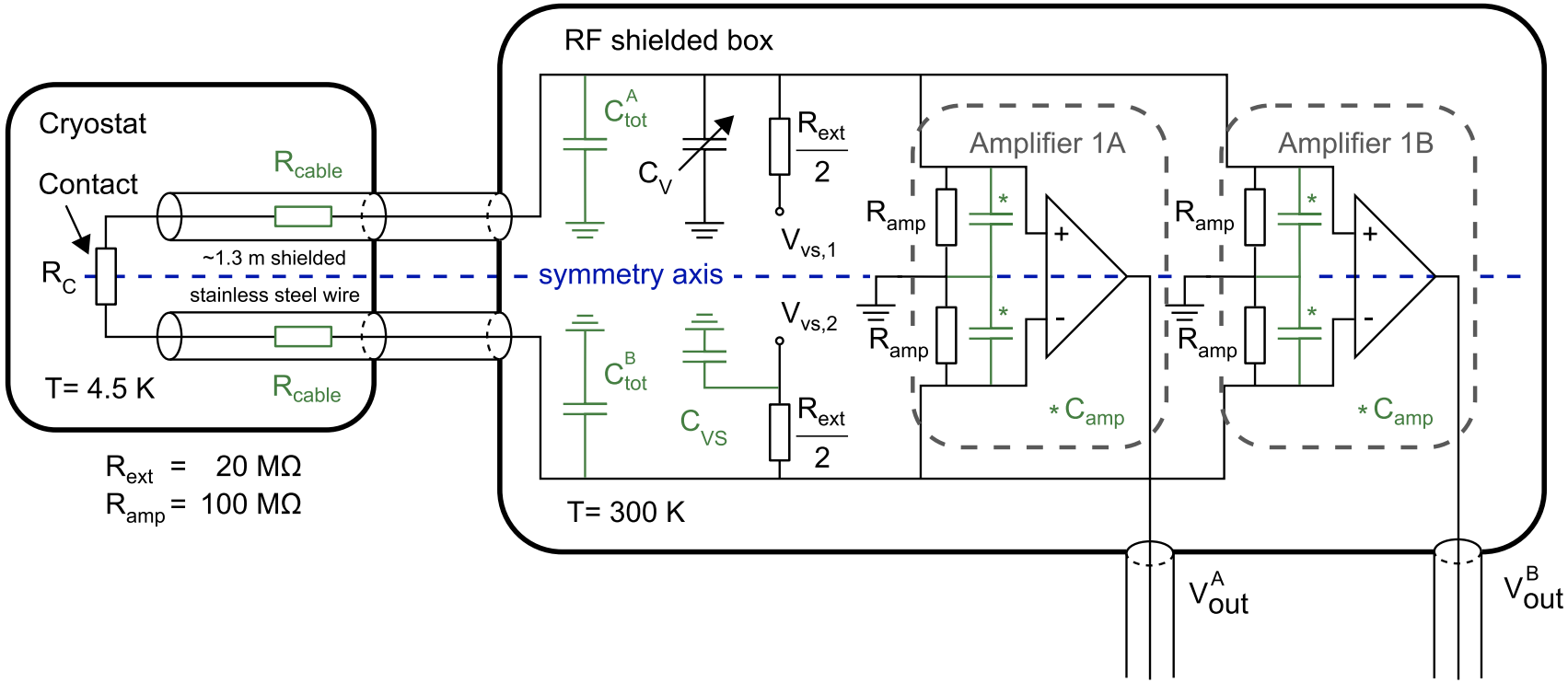

Figure 3.4.: Electronic circuit (black) showing the frontmost part of the measurement setup in noise measurement mode. Equivalent or effective electronic properties are indicated in green. The tip and sample realising the atomic contact inside the STM is contacted using two stainless steel leads with resistance $R_{\mathrm{cable}} = 159\,\Omega$. The total effective capacitances $C^{\mathrm{A}}_{\mathrm{tot}}$ and $C^{\mathrm{B}}_{\mathrm{tot}}$ of the cables describe the combination of the cable capacitance, the amplifiers input capacitances and parasitic capacitances in the switching circuit board. An adjustable capacitor C_V is used to equalize the effective capacitances in both signal paths. $V_{\mathrm{VS},1}$ and $V_{\mathrm{VS},2}$ connect to the adjustable voltage source (see section 3.2.7). The resistance R_{ext} converting the voltage source into a current source is divided equally onto each side of the contact. Thereby the effect of capacitance C_{VS} of the voltage source towards ground onto the signal wires is minimized.

	Home-built amplifiers	LI-75	SR560
Signal gain	100	100	variable
Bandwidth (−3 dB)	2.2 MHz	1 MHz	1 MHz
Eq. input voltage noise	$2.3\,\mathrm{nV}/\sqrt{\mathrm{Hz}}$	$2\,\mathrm{nV}/\sqrt{\mathrm{Hz}}$	$4\,\mathrm{nV}/\sqrt{\mathrm{Hz}}$
Input current noise	$15\,\mathrm{fA}/\sqrt{\mathrm{Hz}}$	not specified	not specified

Table 3.1.: Comparison of the home-built amplifiers used in the measurement setup, the LI-75A voltage amplifier from NF-corporation and the SR560 variable gain amplifier from Stanford Research.

Third, the amplifiers need to be disconnected by additional relays while performing a current measurement with the I/V converter since they have a tendency to oscillate otherwise. These examples highlight the complexity needed to perform the otherwise trivial switching task without side effects.

3.2.6. Home-built first stage amplifiers

Two identical voltage amplifiers were custom designed by the author[3] for the purpose of the shot noise measurement. The circuit design is based on the LI-75A, a low-noise voltage amplifier built by the NF-Corporation, that was used in the previous shot noise experiments by Glattli [2] and van den Brom [3]. The amplifiers were home built for two reasons. First, to fit into the RF-shielded box they were designed for compactness and minimal input signal cable length. Second, home building the amplifiers yielded a maximum control on the input characteristics in terms of noise and input capacitance. In table 3.1 the major characteristics of the amplifiers are compared with the LI-75A as well as the Stanford SR560 variable-gain voltage amplifier. In summary, the home-built amplifiers are on a par or surpass the commercial alternatives in terms of bandwidth and noise performance.

3.2.7. Low-noise current source

The measurement requires the contact to be biased by an adjustable low-noise constant-current source. Furthermore it requires this constant-current source not to interfer with the noise measurement. Therefore it must not generate noise significantly larger than the thermal noise associated with its internal resistance.

[3]The author was assisted in this task by Hans-Joachim Neumann.

In particular, the noise it generates must not be current dependent since subtracting it from the measurement data would be detrimental to the measurement uncertainty. To comply with these requirements an adjustable voltage source was designed and converted to a current source by 20 MΩ resistance in series. In the following the design is explained in detail highlighting the crucial design choices.

A supply voltage V_G was generated by five 9V NiMh rechargeable batteries connected in series. Depending on the charge state of the batteries this yields a supply voltage $V_G \approx 42V$. During a single measurement of $\approx$ 3 minutes the battery discharge leads to a voltage drop of <0.1 %. Shot noise in chemical batteries as used to generate V_G have been shown previously [31] to be suppressed by at least 50dB with regard to the full shot noise $2eI$.

The supply voltage V_G was adjustably divided into 255 linear steps using a 8-bit R-2R-ladder as depicted in figure 3.5. Additionally the polarity was made switchable. Commonly field effect transistor are used as switching elements in a R-2R-ladder. Since semiconducting parts were purposely excluded from the circuits output part, since they generally produce shot noise of their own, the switching inside the R-2R-ladder was performed using bistable relays instead.

The R-2R-ladder in figure 3.5 is constructed of 8 switchable voltage dividers connected in series with each other. For a binary value B of the switching state of the relays as defined according to figure 3.5 an output voltage of $\frac{B}{255}V_G$ is generated. The R-2R-ladder was built using metal-film resistors with R =10 kΩ and 0.1% tolerance. The output resistance of the circuit is R.

To convert the voltage to a current source, a total resistance of R_{ext} = 20 MΩ was connected in series to it. In accordance with the strict demand for symmetry in the signal lines discussed before, two 10 MΩ resistors were connected in series with the voltage source at each of its connectors $V_{VS,1}$ and $V_{VS,2}$ (see also figure 3.4). First, this preserves the symmetry of the signal lines regarding their characteristic. Second, the effect of the voltage source's parasitic capacitance C_{VS} towards ground on the signal lines is minimized. It is essentially decoupled from them[4]. The placement of the resistors turned out to be of paramount importance for performing the measurement task successfully. If the resistors R_{ext} were placed on only one side of the voltage source towards one of the signal lines, then the capacitance $C_{VS} \approx 200\,pF$ of the voltage source towards ground in figure 3.4 would add to the capacitance of the other signal line. Thereby the

[4]Since the frequency response of the measurement system is calibrated as described in section 3.3.2 it is not necessary for the front end section to behave exactly as a first order low pass filter.

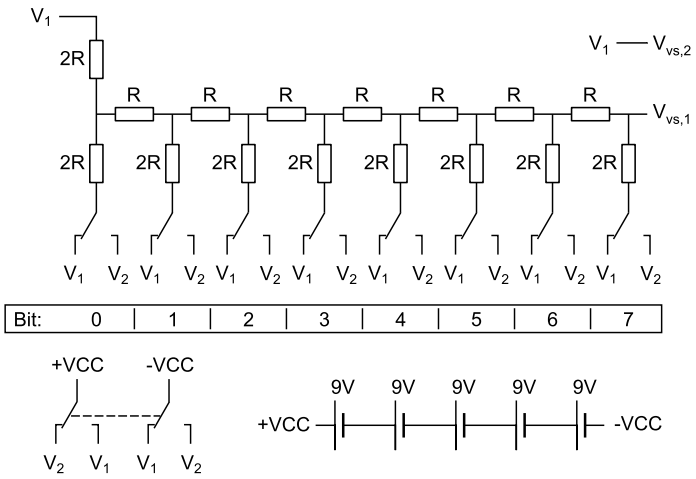

Figure 3.5.: Functional schematic of an 8-bit R-2R-ladder with switchable output polarity as used in the constant-current source. A supply voltage $V_B \approx 42\,V$ is generated between $+VCC$ and $-VCC$ by five 9V rechargeable batteries connected in series. The voltage between V_2 and V_1 is equal to the voltage V_G with switchable polarity. The supply voltage is fed into a series of 8 switchable voltage dividers. The bit value of a relay associated with one of the 8 voltage deviders is defined to be 1 if the relay connects to V_2. For a binary value B of the relays switching states an output voltage between $V_{VS,1}$ and $V_{VS,2}$ of $\frac{B}{255}V_G$ is generated.

aforementioned symmetry in capacitance would be drastically debalanced. This would result in a distorted frequency response and a worsened common mode suppression of the voltage measurement as described in section 3.2.3.

The current dependent noise of the home-built current-source was ensured to be below the overall measurement accuracy.

3.2.8. Choosing ground connections

The quality of the complete measurement apparatus is crucially dependent on how the signal grounds of the different sections are connected with each other. The final design is the result of extensive trial and error with grounding concepts from the literature [32] in mind.

The STM apparatus, STM control electronics and noise measurement equipment are separated from the electric grid protective earth and all electronic devices used during the measurement were isolated from the grid using isolation transformers. A dedicated measurement earth was installed outside the laboratory and the STM apparatus and the protective earth of control electronics were connected in a star like topology.

There are two major ways for interference noise to enter the measurement circuit and deteriorate the noise measurement. The first is a magnetic coupling into the two wires connecting tip and sample with the amplifiers. It can be effectively reduced by minimizing the area that the two wires span. The second is a noise current flowing on the shields of the these two cables. Minimizing these currents mandates a proper grounding concept. To that avail the complete front end including switching circuit, amplifiers and current source was contained in an shielded box that forms an extension of the cryostat. Since all instruments inside the box are battery powered its casing can be isolated from any other shield or ground other than the cryostat itself. The output signals of each of the amplifiers 1A and 1B and the corresponding reference ground were measured differentially by the amplifiers 2A and 2B. In particular, the cable shields did not connect to the ground of amplifiers 2A and 2B so as not to add another ground path. The same applies to the connection between the amplifiers 2A and 2B and the symmetric transmission input in figure 3.1. Since no ground currents can enter or leave the shielded box's casing, none can flow through the sensitive part at the front.

In general any interference noise current flowing on the outside of the cryostat – most critically near the feedthroughs – was found to couple into the measurement signal. Therefore the shields of all cables connecting the cryostat with the control electronics (piezo cables, coarse approach cables and temperature diode cables) were isolated from the cryostat.

Additionally, the wires connected to the temperature diode and the coarse approach piezos, which were not necessary for the noise measurement, were grounded at the feedthroughs since they go near the STM contact and have proven to couple interference noise capacitively into the measurement signal.

Many parts of the noise measurement setup need to be remotely controllable. In minimizing the ground connections between different parts of the measurement setup the control signals must also be galvanically isolated. Therefore the switching subcircuit, the low-noise power supply and the piezo filters are controlled from the oscilloscope via an I^2C-bus that is mediated optically using fibre-optic cables.

3.2.9. Filtering the piezo signals

Besides the electronic noise generated by the transmission process at the atomic contact itself, conductance fluctuations of the atomic contact will also give rise

to voltage fluctuations. There are three origins for the occurance of conductance fluctuations:

1. Mechanical vibrations originating from the experimental setup or its surrounding propagating to the tip-sample-system

2. Mechanical vibrations between tip and sample induced by electronic noise on the piezo signals

3. Fluctuations of the contact geometry at the atomic scale

In order to minimize mechanical vibrations in the experimental setup, the STM was disconnected from the floor and the surrounding air by means of three different damping stages. First, the complete machine was resting on 3 regulated air damping feet to isolate it from the building's body-bound noise. Second, the inner tank containing the liquid helium was detached vibrationally from the other parts of the cryostat again using 3 regulated air damping feet. Third, the complete STM was suspended from 3 springs at the bottom of the inner tank. Additionally the machine was standing on a separated piece of foundation.

Conductance fluctuations can also occur from atomic fluctuations in the vicinity of the contact or at the contact itself. They have previously been shown to exist in atomic contact geometries for on surface atomic rearrangements [33] and tip-sample rearrangements [34]. The presence of such fluctuations can be identified unambigously in the time signals aquired from the contact, provided that their magnitude and the time scale they occur on are within the sensitivity of the measurement setup. Conductance fluctuations will also give rise to a low-frequency component in the noise spectra. Yet the presence of low-frequency component in the noise spectra can not conclusively prove the existence of conductance fluctuations.

With the mechanical damping of the STM working at its peak performance, the vibrations induced by the electronic noise on the piezo signal lines proved to be detrimental to the shot noise measurement. As a countermeasure each of the 5 piezo signals where low-pass filtered towards ground using a first-order low-pass RC-filter with $f_{-3\mathrm{dB}} \approx 2\,\mathrm{Hz}$. Since scanning topographs with these filters in the piezo signal lines would restrict the scan speed considerably, a remote deactivation of the filters was implemented. For that purpose relays were inserted that permitted a short circuiting of the filters' resistors. By switching these relays the filters can thus be toggled active, retaining the signals DC value, i.e. without inducing voltage jumps that might lead to a destruction of the atomic contact.

The control signals for the relays were galvanically isolated via an optical I^2C-bus, to prevent the entry of electromagnetic interferences.

In figure 3.6 the noise spectra of a measurement at a $1.7\,G_0$ Au break junction contact is shown with the piezo filtering enabled (b) and disabled (a). To distinguish the effects of conductance variations from electronic interferences in these spectra two characteristics can be used: First, conductance variations at a frequency f that are small compared to the total conductance have no effect on the spectra aquired at zero bias, i.e. the thermal noise. Second, at non zero bias the variations occur in the noise spectra and they increase proportionally with the applied bias current squared. In figure 3.6 (a) such a behaviour can be seen in the frequency range between 24 kHz and 30 kHz, around 40 kHz as well as in small peaks up to 120 kHz. The most prominent differences between 24 kHz and 30 kHz coincide with resonances of the scanning tube that are excited by the white output noise of the high voltage amplifiers controlling the scanning tube. All of these artifacts are strongly suppressed by enabling the piezo filters in panel (b). Since the spectra are evaluated in the frequency range between 110 and 120 kHz the removal of several smaller peaks at frequencies up to 120 kHz highlights the importance of filtering the scanning tube piezo signals.

3.3. Data analysis and calibration

The two main quantities of interest in the shot noise measurements are the Fano factor F determined from the noise spectra and the contact conductance G. The latter needs some clarification. Within the model used in section 2.3.4 to derive the expressions for shot noise the conductance is assumed to be independent of the applied bias, i.e. a constant dI/dV. In general the dI/dV in contact to an adatom on a surface is not constant. During a shot noise measurement the contact is biased at constant currents in the [-0.5,0.5] μA interval. This corresponds to voltages up to $\approx$16 mV assuming a $0.4\,G_0$ conductance. The differential conductance dI/dV at zero bias was determined from the thermal noise that the contact exhibits at zero bias. Details on this measurement can be found in section 3.3.4. As a consequence, both F and G rely on a precise measurement of the noise spectral densities.

In order to perform the calibration the signal path from the atomic contact inside the STM to the digital storage oscilloscope depicted in figure 3.1 is be divided into two major parts:

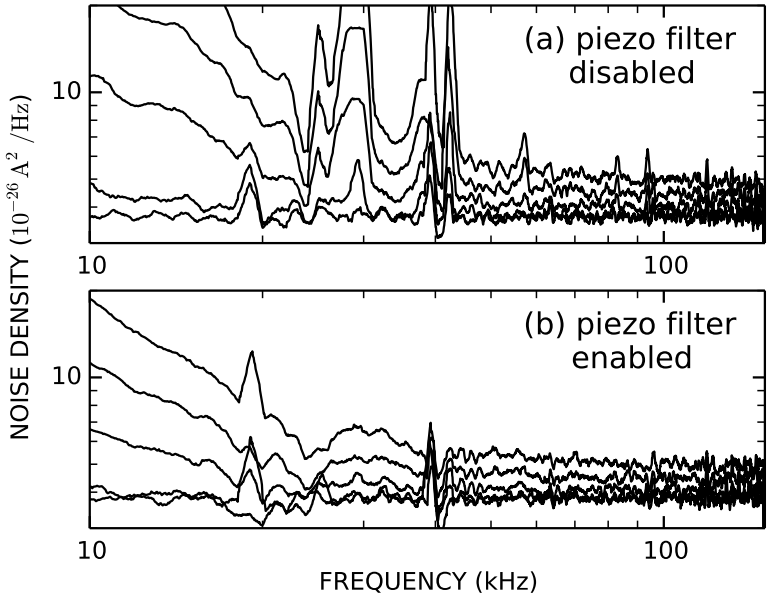

Figure 3.6.: Noise spectra acquired from a 1.7 G_0 Au contact with the scanning tube piezo filters disabled (a) and enabled (b). The most prominent differences are the peaks in the frequency range between 24 kHz and 30 kHz. They coincide with resonances of the scanning tube and are excited by the white output noise of the high voltage amplifiers that control the piezo. Improvement can be seen for frequencies up to $\approx$ 100 kHz.

- The transfer from the atomic contact to the inputs of the voltage amplifiers 1A and 1B in figure 3.1
- The transfer through the chain of amplifiers 1A/B and 2A/B in figure 3.1 as well as the subsequent digital to analog (D/A) conversion in the oscilloscope.

The latter of these is assessed in the following subsection while a correction of the former is explained afterwards.

3.3.1. Calibrating the amplifier chain

The signal path through the amplifier chain of amplifiers A and B was calibrated at the beginning of each measurement session in a straightforward way: A sine wave was fed into the inputs of amplifiers A and B using a function generator. For a range of frequencies the amplitude and phase shift of the signal acquired by the oscilloscope was measured. Based on the amplitude measurement an overall gain

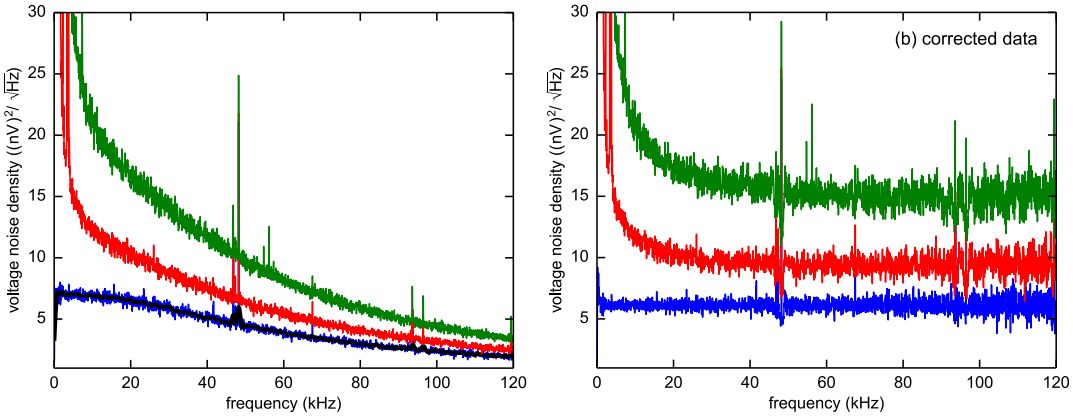

Figure 3.7.: (a) shows the raw cross spectral densities for a $0.58\,G_0$ contact to an Fe atom on Au(111) for bias currents of $0, 0.088, 0.17\,\mu A$ in ascending order. The spectral noise densities are low pass characteristics that increase with the applied bias current. At low frequencies and non-zero biasing current a $1/f$-like noise contributes to the noise spectra. In figure (b) the spectra are corrected using the black smoothed zero bias spectrum in (a) as a reference.

was determined for that particular frequency interval. Every spectrum aquired after the calibration was automatically corrected for the frequency dependent overall gain and phase. This calibration reduces the measurement uncertainty of the entire amplifier chain to the accuracy of the signal generation. The Agilent 33220A function generator used was calibrated using a Picotest 3500A multimeter to 1% accuracy.

3.3.2. Frequency response correction

Since the frequency response from the atomic contact to the amplifier inputs is dependent on the contact conductance, it has to be assessed separately for each of the atomic contacts formed. At zero bias the acquired spectrum reflects the frequency response, since the thermal noise generated by the contact is white in the frequency range under consideration. It was therefore smoothed and taken as the *reference spectrum* $R(f)$ to correct the spectra for non-zero currents. These in turn show a $1/f$-like noise contribution that prohibits their use for precise assessment of the frequency response.

An overview on how the frequency correction was performed is illustrated in figure 3.7. Panel (a) shows raw voltage noise cross spectral densities for a $0.58\,G_0$ Fe contact to an Fe atom on Au(111). The blue spectrum is measured at zero-bias while the red and green one was acquired at bias currents $0.088\,\mu A$ and $0.17\,\mu A$

respectively. In each spectrum the low pass characteristic is clearly visible. To correct for it a smoothed zero-bias spectrum – black spectrum in figure 3.7 (a) – is calculated and used to correct the zero-bias spectrum as well as the spectra at non-zero bias. The results of the correction are shown in subfigure 3.7 (b).

To perform the correction using the reference spectrum the mean spectral noise density $\langle R(f)\rangle_{[1,3\,\mathrm{kHz}]}$ in the frequency interval between 1 kHz and 3 kHz was used as a reference value that is taken to be unaltered by the low pass characteristic.

In order to correct a spectral density $A(f)$ the noise density at each frequency can be multiplied by the ratio of $\langle R(f)\rangle_{[1,3\,\mathrm{kHz}]}$ and the magnitude of the reference spectrum at that frequency. This yields for the corrected spectral density $C(f)$:

$$C(f) = A(f)\frac{\langle R(f)\rangle_{[1,3\,\mathrm{kHz}]}}{R(f)} \tag{3.1}$$

In the above expression it is neglected however that the filter characteric is not exactly a first order low pass one. The cable resistance R_{cable} =159 Ω of the stainless-steel wires also generates thermal noise. Therefore variables O and B are introduced, that account for this effect. They are determined from calibration measurements that are described in the following subsection. The offset O is subtracted from all spectra in 3.1 prior to the division:

$$C(f) = (A(f) - O)\frac{\Big(\langle R(f)\rangle_{[1,3\,\mathrm{kHz}]} - O\Big)}{(R(f) - O)}B \tag{3.2}$$

Both the offset O and the factor B is determined in a calibration measurement that is described in the following subsection.

3.3.3. Calibrating the frequency response correction

The signal path from the atomic contact inside the STM to the amplifier inputs cannot be calibrated by simple straightforward means. Its transfer characteristics crucially depends on the capacitance of the cables that connect the tip and the sample with the feedthroughs as discussed in section 3.2.2. Connecting a function generator to either tip or sample would alter these capacitances by at least the output capacitance of the function generator. Therefore the transfer characteristic thus measured would yield bogus results. Instead SMD sized metal-film resistors with resistances of ≈10 kΩ, ≈20 kΩ and ≈30 kΩ were attached to sample holders. For each of the resistors one of its leads was glued to the sample

holder using conductive glue while the other was pointing away from it. The resistors were inserted into the STM one by one and their outward pointing lead was contacted by the tip. The thermal noise generated by these resistors is known to be white in the frequency range under consideration (<200 kHz) [16]. Its source resistance is given by the resistance of the SMD resistor. By altering the temperature of the resistor inside the STM from 4.5 K to ≈11 K the voltage noise density generated by the resistor can be increased. In summary, the resistors are white noise sources with variable voltage noise density and fixed source resistance.

To calibrate and verify the frequency response correction described in the previous subsection cross spectral densities of the thermal noise were acquired a different temperatures. The spectral density for the lowest temperature of 4.6 K was smoothed and used as the reference spectrum to correct the spectral densities at higher temperature. Throughout the complete analysis a special focus was laid on the frequency intervall between 110 kHz and 120 kHz, where the noise measurements at the atomic contacts were evaluated. The offset O was choosen as 9.8e-10 $\mathrm{nV}/\sqrt{\mathrm{Hz}}$ and $B = 0.96$ such that the difference between the mean spectral densities in the frequency interval between 110 kHz and 120 kHz did not deviate from those in the frequency interval between 1 kHz and 3 kHz by more than ≈4 %. Therefore the measurement uncertainty associated with this correction in the aforementioned interval particular interval is set to $r_{correction} = 4\%$.

3.3.4. Conductance calibration

To compare the measured voltage noise density with theory it is necessary to convert it to a current noise density. Therefore the differential conductance of the atomic contact needs to be determined. The differential conductance at zero bias was determined from the thermal noise it generated.

The details on the conversion from thermal noise to conductance can be found in the appendix A. For calibration the thermal noise measurements performed on SMD resistor inside the STM discussed in section 3.3.3 were used. The results are summarised in table 3.2. For a 10 kΩ, 20 kΩ and a 30 kΩ resistor the resistance R_R at the STM base temperature of 4.6 K were determined in a four point measurement using a Keithley precision multimeter with the cable resistance of 159 Ω subtracted. The corresponding conductance in units of G_0 are listed in the second column. The third and fourth columns contain the conductances

R_{R} (Ω)	G_{R} (G_0)	G_{thermal} (G_0)	$(G_{\mathrm{thermal}} - G_{\mathrm{R}})/G_{\mathrm{R}}$ (%)
34068	0.379	0.380	0.4
20027	0.644	0.642	−0.3
13488	0.957	0.927	−3.1

Table 3.2.: Comparison between the direct measurement of the conductance G_{R} of SMD sized resistors inside the STM at 4.6 K and the conductance G_{thermal} determined from the thermal noise of these resistors. The maximum relative deviation between the two is 3.1 %.

calculated from the thermal noise and percentual deviation from the conductance measured using the multimeter. The conductances calculated from the thermal noise reproduce the conductances obtained by direct measurement well with a maximum deviation of 3.1 %. Nevertheless to account for small changes in temperature the overall uncertainty of the conductance measurement is set to $r_{\mathrm{conductance}} = 5\%$.

3.3.5. Convergence

The aim of the cross spectrum method is to suppress the voltage noise contributions of the amplifiers so as to retain the voltage noise stemming from the atomic contact, as described in section 2.5. For all measurements show in section 3, an average over 1024 cross spectra was performed for each voltage noise spectrum. To verify that 1024 averages are enough the Fano factor has been determined from spectra obtained by averaging over $0, 50, 100, ..., 1000$ cross spectral densities. In figure 3.8 the relative difference of these Fano factors with respect to the Fano factor obtained for averaging over 1000 cross spectra is displayed for different atomic contacts. In all cases shown the Fano factor is converged to well below 1 %.

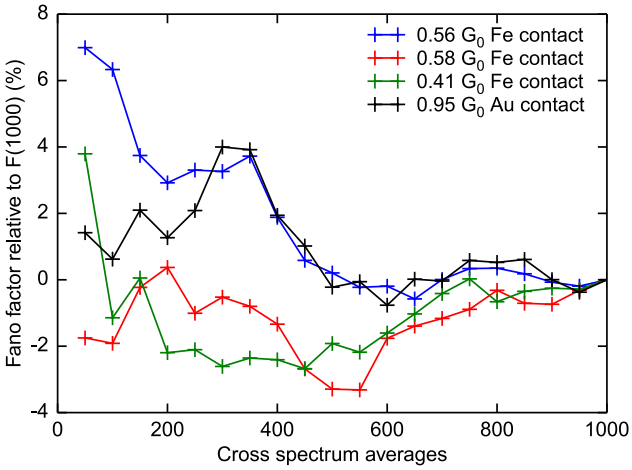

Figure 3.8.: Fano factor determined from cross spectra obtained with increasing number of averages. The Fano factor determined from cross spectra using 1000 averages is converged to better than 1 %.

4. Measurement results

In this chapter results from shot noise measurements at single atom contacts to Au, Fe and Co adatoms on a Au(111)-surface with a Au coated W tip are presented. To the best of my knowledge, these measurements are the first shot noise measurements performed using an STM with contact conductances larger than $0.1\,G_0$. In particular, they are the first shot noise measurements performed at atomic contacts having well-defined contact geometries and involving atoms from more than one species, i.e. inhomogeneous contacts. In view of the possibility to indentify a spin-polarisation of the transport channels, the magnetic Fe and Co atoms were chosen as adsorbates. Indeed, some of the shot noise measurements at contacts to both Fe and Co adatoms show indications of a spin-polarisation of the transport channels[1] when contacted on a Au(111)-surface with a Au coated tip.

4.1. The Au(111) substrate

Au was chosen as tip and sample material since it was known to show favourable properties during single atom contact formations [3, 4]. First, contact formation in pure Au contact geometries shows a jump-to-contact behaviour that is illustrated and explained in figure 4.1. It is commonly attributed to geometric relaxations of the tip apex atom [35]. This is favourable to the shot noise measurement since the conductance does not change notably for small movements of the tip with respect to the sample. Second, contacts formed from Au show a higher long term stability as compared to those formed using for example Cu. For inhomogeneous contacts to Fe and Co adatoms the favourable behaviour was reproduced.

The Au(111) surface used as substrat for all measurements presented in this thesis shows the well known $22 \times \sqrt{3}$ herringbone reconstruction [36]. This

[1] The spin-polarisation is derived from the analysis of the shot noise data using the theoretical model of shot noise described in the theory chapter 2.3.4.

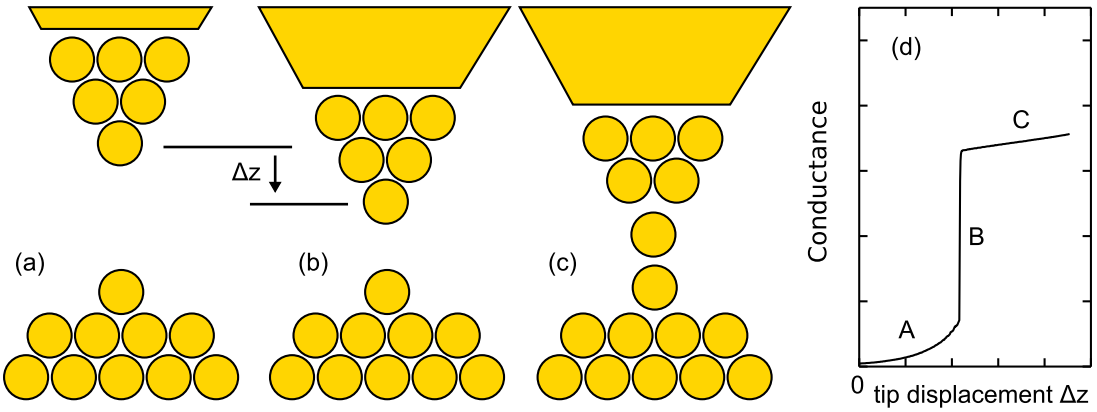

Figure 4.1.: Illustration of contact formation and conductance curve in the case of a jump-to-contact behaviour. (a) shows the tip initially being at tunnelling distance from an adatom on a surface. When the tip is moved towards the adatom (b) the displacement from its initial position is denoted by Δz. In (c) the tip apex atom forms a covalent bond with the adatom. For Au tips the contact formation is accompanied by a jump in the conductance that is commonly attributed to relaxations of the tip apex atom [35]. This jump-to-contact behaviour leads to a common pattern in the conductance-curve (d). There, the dependence of the conductance with the tip displacement Δz is exponential (A) while the tip is at tunnelling distance from the adatom (subfigure (a)). The conductance jumps (B) due to the formation of the covalent bond between tip apex atom and adatom accompanied by geometric relaxations. With the bond formed (C) the dependence of conductance and displacement is often linear with a comparatively shallow slope (subfigure (c)).

reconstruction introduces a diversity in terms of absorption site geometries, (fcc-stacking, hcp-stacking, wall region)

Moreover, the herringbone reconstruction induces an electronic superlattice on the surface. This was shown by Chen et al. [38] to be due to the surface state at -0.48 eV. Libisch et al. [37] extended the observations by showing lateral periodic oscillations in the dI/dV-map at energies up to 250 mV as displayed in figure 4.2. According to the authors the oscillations occur parallel to the reconstructions lines at energies between -150 mV and 250 mV. They are not restricted to either of the stacking sites. Consequently, these spatial oscillations exist at bias voltages ± 15 mV around the Fermi energy where the shot noise measurements are performed. Therefore, they may induce a dependence of the conductance and Fano factor measured at an adatom on its position with respect to the herringbone reconstruction. Furthermore, they may be at the origin for the spread in conductance and Fano factor found for Fe adatoms shown in section 4.5.

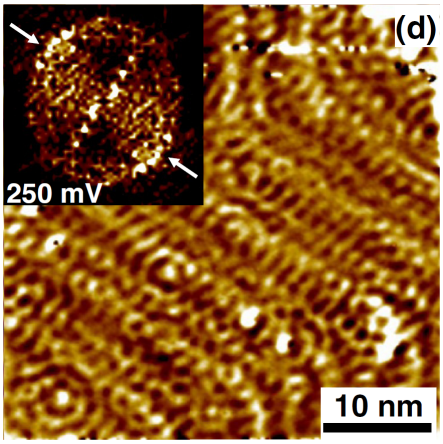

Figure 4.2.: dI/dV-map of the Au(111) surface at $V_{\text{bias}} = 250\,\text{mV}$, adopted from [37]. On the large scale the herringbone reconstruction can be identified from lines in the direction from the upper left corner to the lower right corner. On the finer scale two forms of ripples can be discriminated: Periodic oscillations in the direction parallel to the herringbone reconstruction lines and radial oscillations due to defect scattering. The inset shows an FFT transform of the dI/dV-map. Positions marked by the arrows correspond to the lateral oscillation.

Despite the discussed adsorption site dependence of the electronic and geometric properties the favourable jump-to-contact behaviour and the contact stability make it the preferred choice for shot noise measurements.

4.2. Tip and sample preparation

Au(111) single crystal surfaces were prepared by cycles of Ar-ion sputtering and annealing. Tips were etched from W wire and prepared in UHV by annealing and Ar ion bombardment. After mounting the tip into the STM it was indented into the Au crystal to coat its apex with gold. Finally, the sample was contacted until single Au atoms were deposited from the tip and the contacts were stable with $G \approx G_0$. Moreover, the presence of the Au(111) surface state in dI/dV spectra on the bare surface was verified.

4.3. Measurement procedure

Before each measurement the tip was prepared in-situ using either of two methods. In the first method the surface was gently contacted with the tip until deposition of tip material onto the surface occured. The deposition of single Au

atoms onto the surface was taken as an indicator for tip stability. The second method followed [39]. After deposition of material from the tip to the surface the tip repeatedly contacted the deposited material until conductance-curves becomes reproducible. On average both methods required hours before the tip matched their criteria for tip stability.

Fe and Co were never evaporated together onto the Au(111) surface. Nevertheless measures were taken to discriminate them from possible contaminations. Co adatoms on Au(111) are known to show a Kondo signature in their dI/dV if they are adsorbed at an fcc-stacking or hcp-stacking site of the herringbone reconstruction [40]. Therefore, to identify Co adatoms on these two stacking sites dI/dV spectra acquired with the tip in the tunnelling range above the atom were required to show a Kondo resonance. dI/dV spectra acquired with the same tip above the bare surface was verified not to show a significant Kondo resonance. On wall sites the Kondo signature of Co adatoms is absent or strongly suppressed [40] and thus Co adatoms on wall sites were not studied. Since Fe adatoms on Au(111) do not show a Kondo signature they were identified using their apparent height of $\approx 130\,\mathrm{pm}$ at a bias voltage of $128\,\mathrm{mV}$.

Starting with the tip at tunnelling distance from the adatom a conductance curve was acquired. With a high likelihood the tip changed resulting in a deposition of tip material onto the surface. In that case the measurement procedure had to be restarted from the beginning, including tip preparation. The conductance curves showed a jump-to-contact behaviour as illustrated in figure 4.1 with a flat conductance plateau for all examined systems. A displacement Δz was chosen on the conductance curve in the range of the conductance plateau, several 10 pm from its onset.

Before contacting the adatom in order to perform the shot noise measurement the tip was precisely centered above the atom using an automated script. Furthermore, despite a constant voltage being applied to the scanner piezo the tip could slowly creep both laterally and perpendicular to the surface. There are two reasons for this effect. First, when the voltage applied to the scanner-piezo is changed the piezo does not immediately adopt the associated mechanical form. Especially after large voltage changes from large tip movement this can require a settlement time of several minutes. Second, the tip can creep from thermal expansion or contraction due to the STM not having reached thermal equilibrum. Consequently, the time it takes for the creep to be reduced to a minimum depends on the time since the tip and sample were inserted into the STM, the

last filling and the scanning history. It could take from up to 90 minutes for the creep to settle to such a degree, so as to enable stable contact formation for up to 50 minutes.

A contact between the tip and the adatom was controllably established by pushing the tip forward a distance Δz. Again, during contact formation the system was prone to breakage which would require a restart of the measurement procedure. A set of values was consecutively applied to the low-noise current source (see section 3.2.7) resulting in the contact being biased at different constant currents. For each value the current was measured and subsequently the noise spectra were acquired as described in section 3.3. The acquisition took $\approx$3 min for each current value. The complete noise measurement took approximately 25 to 50 minutes depending on the number of bias current values acquired and whether one or both bias polarities were measured. During the noise measurement the contact could either break or drift apart often requiring a restart of the measurement. Finally, the tip was detached from the adatom and a final topograph was acquired so as to verify that the adatom and the surface had not changed notably. Again, detaching often resulted in a deposition of material from the tip requiring a restart of the measurement.

From the spectra the excess noise was calculated and its dependence on the bias current was fit using the Lesovik expression 2.16 introduced in section 2.3.4. The Fano factor was extracted from this fit. The differential conductance at zero bias was calculated from the thermal noise as described in section 3.3.4.

4.4. Shot noise at Au adatoms

By gently contacting the surface with the Au coated tip single Au atoms were deposited onto it. An example of two thus deposited Au atoms is shown in the topograph 4.3 (a). Both atoms are adsorbed on an fcc-stacking site of the herringbone reconstruction. After positioning the tip above the right adatom the feedback loop was turned of and the right atom was approached by the tip. The conductance curve acquired is visualized in 4.3 (b). From an exponential behaviour in the tunnelling range the conductance jumps at $\Delta z = 57$ pm to a plateau with a conductance of $\approx 0.95\, G_0$. This jump defines the formation of a contact to the adatom.

A shot noise measurement was performed while the tip was in contact with the adatom as described in section 4.3. The dependence of the measured ex-

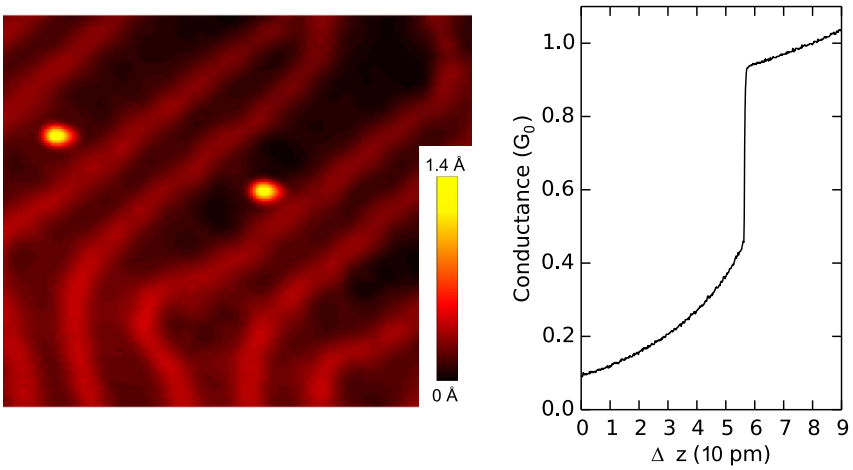

Figure 4.3.: (a) Topograph of two Au adatoms (32.8 nm × 27.4 nm, $V_t = 129$ mV, $I_t = 50$ pA). (b) Conductance curve acquired with 128 mV bias voltage at the right atom shows a jump-to-contact behaviour as explained in figure 4.1.

cess current noise power density with the applied bias current is displayed in figure 4.4. It increases almost linearly with the bias current and a fit of the Lesovik expression 2.16 to the data yields an excellent agreement. The conductance G, Fano factor F and temperature T for that particular contact are: $G = 0.95\,G_0$, $F = 0.08$, $T = 7.1$ K. For reference the theoretical dependence of noise current power density and bias current according to the same expression is plotted for a Fano factor $F = 0.1$ at zero temperature.

An overview of Fano factors extracted from the fits and the contact conductance extracted from the thermal noise for all stable Au adatom contacts is given in figure 4.5. The results cluster in the vicinity of the dashed line indicating the minimum Fano factor possible assuming spin-degenerate transport channels. This reproduces the behaviour previously observed in MCBJ setups [3] which is explained by Au having a single spin-degenerate transport channel only.

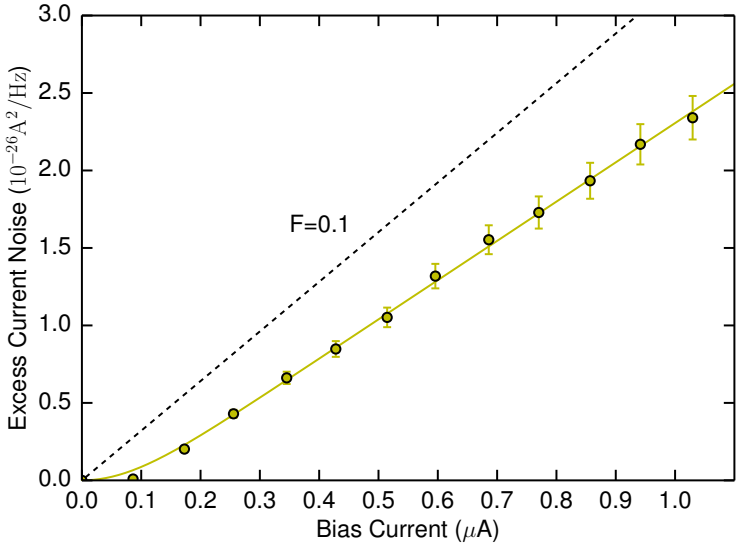

Figure 4.4.: Excess current noise density vs. applied bias current in contact to a Au adatom on a Au(111)-surface. The solid line is a fit of the Lesovik expression 2.16 to the data. An excellent agreement with the measured noise is observed. Error bars are indicate a relative error of $\pm 6\,\%$. Dashed line indicates the theoretical excess noise for a Fano factor $F = 0.1$ and zero temperature.

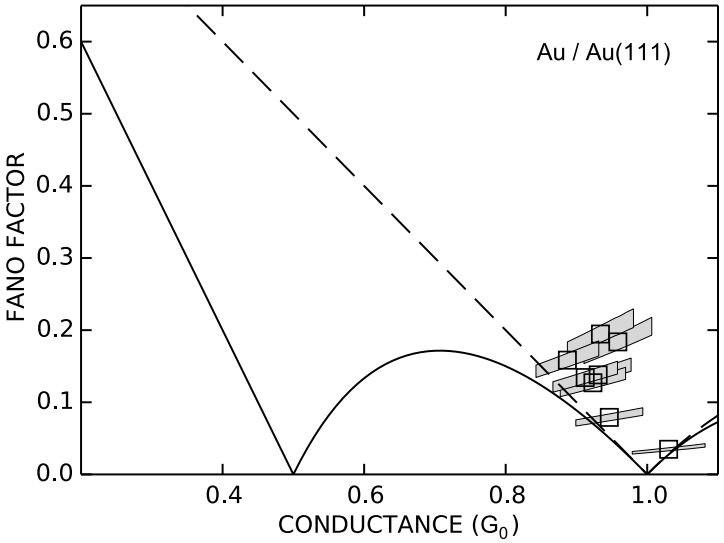

Figure 4.5.: Fano factor vs. conductance for contacts to Au adatoms on a Au(111) surface. Black dashed (solid) line shows the minimum Fano factor possible for spin-degenerate (spin-polarised) transport. For each measurement the grey area surrounding it indicates the measurement uncertainty. All measurements cluster in the vicinity of the dashed line suggesting a single spin-degenerate transport channel.

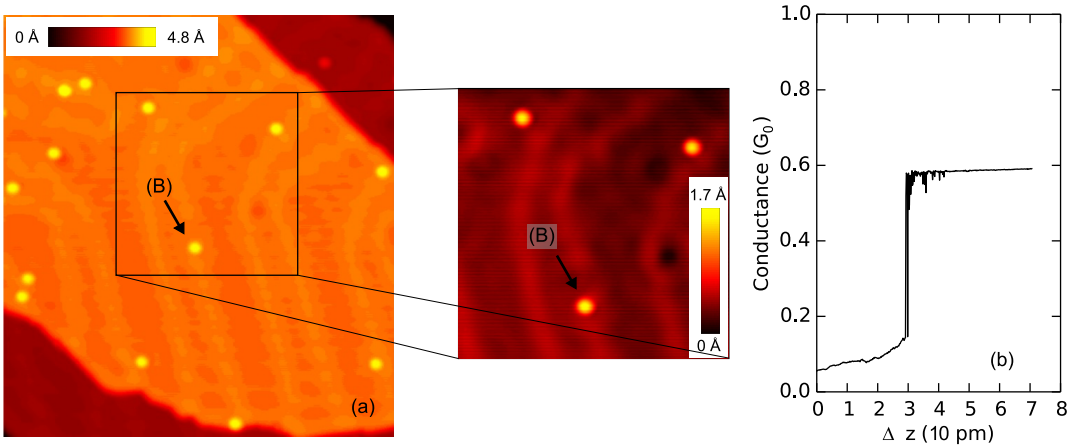

Figure 4.6.: (a) Topograph of Fe adatom (B) on a Au island (46.5 nm × 50.2 nm, $V_t = 128$ mV, $I_t = 50$ pA). (b) Conductance curve with 128 mV bias at atom (B) shows a level conductance plateau. Subsequent shot noise measurements suggest a spin-polarisation of the conductance channels, see figure 4.9 and text.

4.5. Shot noise at Fe adatoms

In order to perform shot noise measurements at contacts to single Fe adatoms a Au coated W tip and a Au(111) surface were prepared according to section 4.2. Fe atoms were evaporated onto the surface by heating an iron filament. During the evaporation the sample was inside the STM and kept at a temperature of less than <20 K. As a result of this cold evaporation the sublimed Fe atoms would stick to the surface on impact and not diffuse to form clusters or islands. Single Fe adatoms on the Au(111) surface were identified in the topographs by having a round shape and a common apparent height of $\approx 132 \pm 10$ pm. Shot noise measurements were performed at five different systems following the procedure described in section 4.3. For each system the excess noise was measured for either one or both bias polarities.

Figures 4.7 and 4.6 give an overview on a contact to an Fe atom that we will identify with B. Topograph 4.6 (a) shows parts of an Au island that is approximately 45 nm wide. On the island the herringbone reconstruction can be identified. Fe atom B is adsorbed centrally on the island in a wall site region of the herringbone reconstruction. It has an apparent height of 132 pm[2]. The conductance diagram acquired from contacting atom B is displayed in figure 4.6 (b) and shows a jump-to-contact with a flat plateau of $0.59\,G_0$. This is

[2] at $V_{bias} = 128$ mV

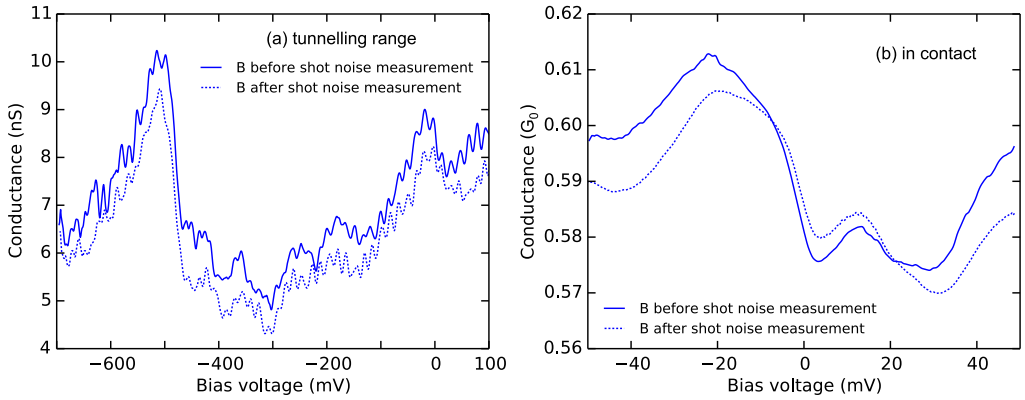

Figure 4.7.: dI/dV spectra acquired at a single Fe adatom (B) on a Au(111) surface before (straight line) and after (dashed line) the shot noise measurement (a) in tunnelling range ($V_t = 128\,\mathrm{mV}$, $I_t = 50\,\mathrm{pA}$, lock-in amplitude 1 mV, sensitivity 5 mV) and
(b) in contact ($V_t = 128\,\mathrm{mV}$, lock-in amplitude 1 mV, sensitivity 10 mV). The differences are minute which indicate that the electronic properties of the adatom were not changed by the shot noise measurement.

considerably smaller than the $0.95\,G_0$ conductance measured at the Au adatom in figure 4.3. Furthermore, the conductance plateau is almost perfectly flat with 0.2 % change in conductance per 10 pm in an unusually large range of 40 pm. In figure 4.7 dI/dV spectra acquired at adatom B are shown for the tunnelling range as well as in contact. The latter was acquired at a contact to the adatom formed subsequently to the noise measurement. The spectrum in the tunnelling range as well as the one in contact remain virtually unchanged after the noise measurement.

Figure 4.8 shows a plot of the excess current noise power density with the applied bias current for all stable contacts to Fe adatoms. The data for each contact was fit using the Lesovik expression 2.16. An excellent agreement is observed. The theoretical dependence for Fano factors $F = 1$ and $F = 0.1$ at zero temperature are included as dashed lines for reference.

In table 4.1 the Fano factors and temperatures acquired from the fits as well as the contact conductance determined from the thermal noise are listed. Identifiers A-E are assigned to the different systems. The conductance ranges from $0.39\,G_0$ to $0.70\,G_0$ and Fano factors from 0.30 to 0.53. The large scattering in the conductance is in contrast to the small conductance spread in the Au contacts. In combination with the spread of the Fano factors this indicates significant differences regarding the transport characteristics. Possible reasons for this di-

Identifier	Bias polarity	Conductance (G_0)	Fano factor	Temperature (K)	nearest-neighbour distance (nm)
B	+	0.57	0.37	5.82	
B	−	0.57	0.35	4.91	
D	+	0.67	0.34	6.61	
C	+	0.58	0.41	5.26	
AU	+	0.41	0.47	4.73	2.1
AU	−	0.39	0.51	6.12	2.1
AL	+	0.39	0.51	5.71	2.1
AL	−	0.39	0.53	5.30	2.1
AU2	+	0.40	0.50	5.94	$1.75 - 1.61$
E	+	0.70	0.30	5.43	
E	−	0.70	0.31	5.43	

Table 4.1.: Results from shot noise measurements at single Fe adatoms on a Au(111) surface are listed. Identifiers AU, AL indicated shot noise measurements at the upper and lower Fe adatom on a terrace, respectively. A subsequent second contact to the upper Fe adatom is labelled AU2. See text for details. Conductances were determined from the thermal noise. Fano factor and temperature were obtained from fits of the Lesovik expression (eq. 2.16) to the excess noise data in figure 4.8. See figure 4.9 and text for a visualisation and interpretation.

versity include differences of the local geometric structure of the tip as well as the adsorption sites. The latter may be geometric differences of the fcc- and hcp-adsorption sites on the Au(111) surface or geometric differences stemming from the position of the adsorption site with respect to the herringbone reconstruction. Furthermore, the lateral oscillatory behaviour of the local density-of-states (LDOS) described in section 4.1 might contribute to the spread observed in the measurements.

To further interpret the data set, Fano factors and conductances are plotted for each measurement in figure 4.9. Their position in that diagram can yield information on the number of conductance channels involved as well as their spin-polarisation as explained in section 2.3.4. The measurements at contacts C, D and E are close to or on the line that indicates the minimum Fano factor possible for spin-degenerate transport channels. This indicates either a single spin-degenerate channel or more than two spin channels being involved. Measurements at contacts A and B are significantly below this line and thus suggest a spin-polarisation of the transport channels. The temperature parameters determined from the fits are reasonably close to the measured temperature of the STM of 4.5 K.

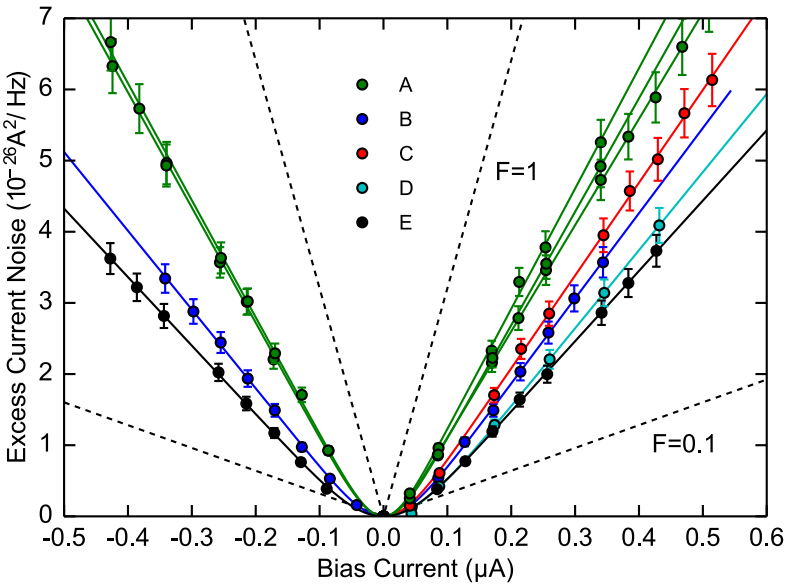

Figure 4.8.: Excess current noise density vs. the applied bias current for contacts to Fe adatoms on a Au(111)-surface. Solid lines are fits of the Lesovik expression 2.16 to the data. An excellent agreement with the measured noise is observed. Fano factors and temperatures from the fit are listed in table 4.1 and visualised in figure 4.9.

In the following, the measurements identified with (AU),(AL) and (AU2) will be discussed in more detail since they set themselves apart from the other measurements. They were performed at two Fe atoms on a 8 nm wide terrace of the Au(111)-surface a topograph of which is shown in figure 4.10 (a). First, the upper atom was contacted and shot noise measurement (AU) was acquired. Next, measurement (AL) was performed in contact to the lower atom. Finally, a second contact to the upper atom yielded measurement (AU2). The three measurements were acquired without any apparent changes to the tip apex microstructure. Their Fano factors and conductances are reproducibly within the region that suggests spin-polarised transport in figure 4.9. They share a low conductivity of $\approx 0.4\,G_0$ and high Fano factor of ≈ 0.51 that both differ considerably from the measurements performed at contacts to other Fe adatoms. The distance between the two Fe atoms was 2.1 nm and changed spontaneously to ≈ 1.7 nm before the last measurement (AU2). The distance between the two Fe atoms was 2.1 nm in measurements (AU) and (AL). It changed to 1.75 nm before and to 1.61 nm during the last measurement (AU2). In particular, measurement (AU) at the upper atom showed a significant difference between the Fano factor

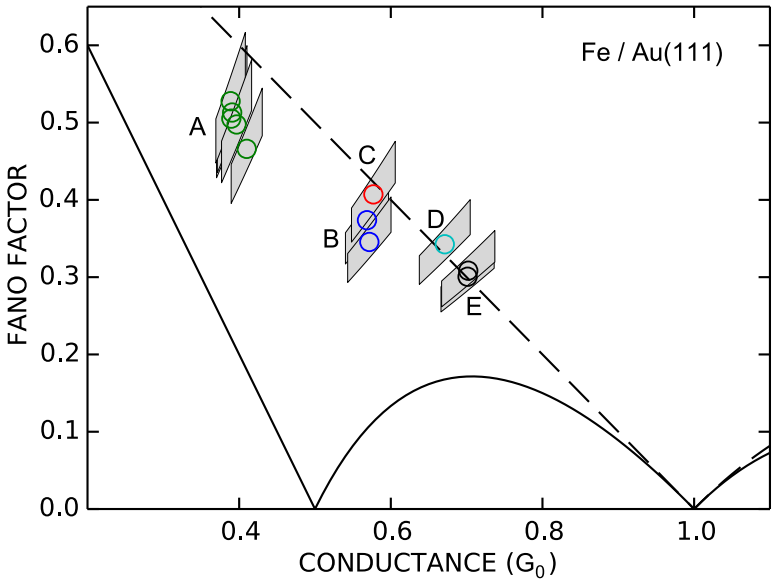

Figure 4.9.: Fano factor vs. conductance for contacts to Fe adatoms on a Au(111) surface. Black dashed (solid) line shows the minimum Fano factor possible for spin-degenerate (spin-polarised) transport. For each measurement the grey area surrounding it indicates the measurement uncertainty. Measurements at contacts A and B are below the minimum Fano factor possible for spin-degenerate transport channels and thus suggest a spin-polarisation of the transport channels.

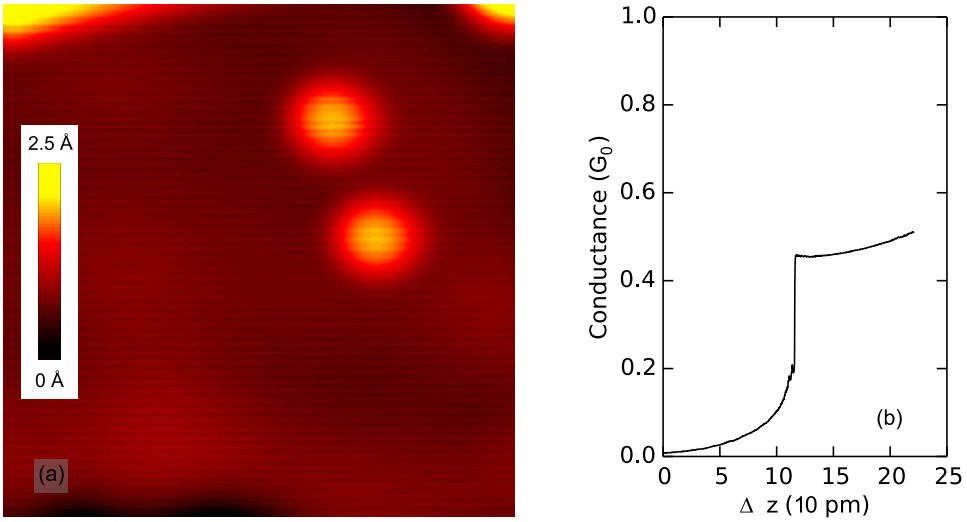

Figure 4.10.: (a) Constant current topograph of two Fe adatoms on a Au(111)-terrace. At the upper (lower) atom shot noise measurements labelled AU and AU2 (AL) were performed. ($8.3\,\mathrm{nm}\times 8.3\,\mathrm{nm}, V_t = 128\,\mathrm{mV}, I_t = 50\,\mathrm{pA}$) (b) Conductance while contacting the lower atom ($V_t = 128\,\mathrm{mV}$).

obtained for positive sample bias (0.47) and the one obtained for negative bias (0.51) of 8 %.

While a definite reason for the deviation of measurements (AU), (AL) and (AU2) cannot be established from the limited set of data available it is instructive to discuss possible factors. First, the surface state is known to be scattered at the two step edges that limit the terrace forming a standing wave pattern. An influence of the surface state within the energy range used for the shot noise measurements has been motivated in [38, 37]. Second, at a distance of 2.1 nm an influence of the neighbouring Fe atom on the shot noise measurement should be considered. Fe being a magnetic atom can couple via the Au conduction electrons to a second Fe atom by means of the Ruderman–Kittel–Kasuya–Yosida (RKKY) interaction [41, 42, 43]. For Co adatoms on a Pt(111)-surface the distance dependence of this interaction has been studied in [44]. The authors find a non-zero coupling up to the maximum adatom distance of 1.21 nm examined in the experiment. Therefore, a coupling at distances of the measurements (AU), (AL) and (AU2) seems plausible. Finally, the geometry of the tip apex could make a difference. The tip used in the particular set of measurements remained stable after several contacts to the clean Au(111)-surface without the deposition of atoms or clusters. Furthermore, it remained stable for five consecutive contact formations and shot noise measurements. This stability is at stark contrast to the behaviour observed for other tip apex microstructures, neither of them remained stable for more than one contact formation. The peculiar tip geometry and thus the electronic structure of its apex atoms could also be at the origin of the lower conductance, the higher Fano factor and the spin-polarised transport observed.

4.6. Shot noise at Co adatoms

In order to perform shot noise measurements at contacts to single Co adatoms a Au coated W tip and a Au(111) surface were prepared according to section 4.2. Co atoms were evaporated onto the surface using an electron beam evaporator. During the evaporation the sample was inside the STM and kept at a temperature of less than $<$20 K. To identify single Co adatoms on the Au(111) surface dI/dV spectra were required to show a Kondo signature [45]. Their apparent height was between $113 - 128$ pm.

Figure 4.11 (a) shows a plot of the excess current noise power density with the applied bias current for all stable contacts to Co adatoms on a Au(111)-surface. The data for each contact was fit using the Lesovik expression 2.16. Again, an excellent agreement is observed. The theoretical dependence for Fano factors $F = 1$ and $F = 0.1$ at zero temperature are included as dashed lines for reference.

In table 4.2 the Fano factors and temperatures acquired from the fit as well as the contact conductance determined from the thermal noise are listed. To interpret the data set, the Fano factors are plotted against the conductances in figure 4.12. The measurement at contact A is significantly below the dashed line indicating the minimum Fano factor possible for spin-degenerate transport channels. It thus indicates a spin-polarisation of the transport channels. Measurements to contact C is significantly above the dashed line indicating that at least three spin channels are involved in the transport process. Contact B is slightly below the dashed line suggesting spin-polarised transport channels with high uncertainty.

The temperature parameters determined from the fits for contacts A and B are $\approx$ 7 K and thus larger than those obtained for Fe contacts and larger than the measured the STM temperature of 4.5 K. Several reasons are conceivable for this behaviour. First, assuming the validity of the model described in section 2.3.4 for the contact to the Co adatom the temperature defined within it is the electronic temperature. The local electronic temperature can deviate from the phononic temperature measured by the temperature diode in the STM through transport induced local heating. Second, large changes in the differential conductance with the applied bias neglected in the data analysis could influence temperature parameters. Third, the transport model underlying the Lesovik expression may be inadequate to describe the transport process and the shot noise generation in the presence of the Kondo effect.

In figure 4.11 (b) dI/dV spectra at Co adatoms in the tunnelling range are

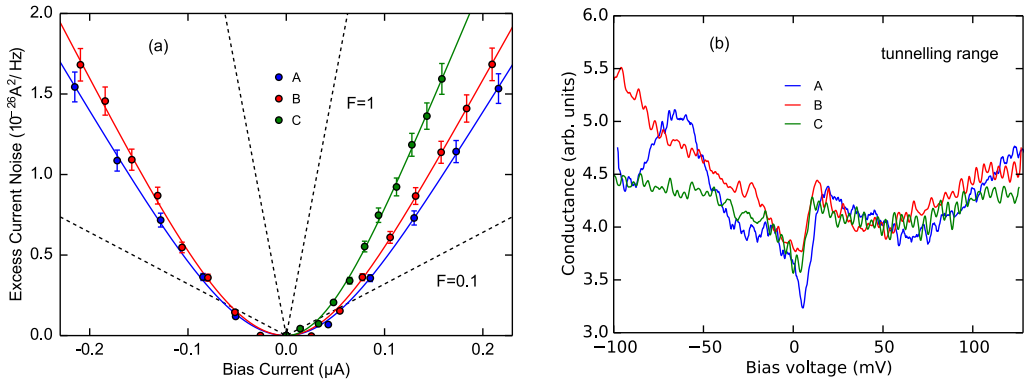

Figure 4.11.: (a) Excess current noise density vs. the applied bias current for contacts to Co adatoms on a Au(111)-surface. Solid lines are fits of the Lesovik expression 2.16 to the data. An excellent agreement with the measured noise is observed. Fano factors and temperatures from the fit are listed in table 4.2 and visualised in figure 4.12. (b) dI/dV spectra at Co adatoms in the tunnelling range showing a Kondo signature around zero bias. The color scale of (a) applies. ($V_t = 128\,\mathrm{mV}$, $I_t = 0.5\,\mathrm{nA}$, lock-in amplitude 1 mV, sensitivity 5 mV)

Identifier	Bias polarity	Conductance (G_0)	Fano factor	Temperature (K)
A	+	0.61	0.31	7.25
A	−	0.61	0.32	7.96
B	+	0.63	0.37	7.74
B	−	0.63	0.34	6.53
C	+	0.67	0.45	5.5

Table 4.2.: Shot noise measurements at single Co adatoms on a Au(111) surface. Fano factor and temperature were obtained by fitting the Lesovik expression (eq. 2.16) to the excess noise data in figure 4.11 (a).

shown. Around zeros bias the well known Kondo signature [40] can be identified.

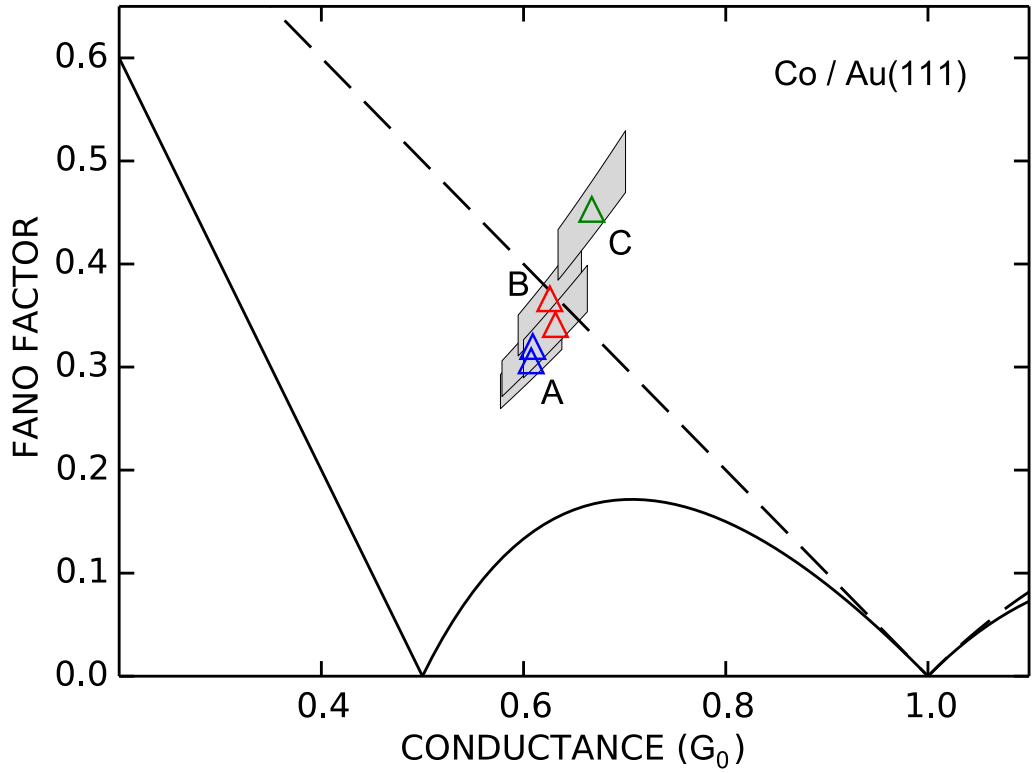

Figure 4.12.: Fano factor vs. conductance for contacts to Co adatoms on a Au(111) surface. Black dashed (solid) line shows the minimum Fano factor possible for spin-degenerate (spin-polarised) transport. For each measurement the grey area surrounding it indicates the measurement uncertainty. Measurements at contact A are below the minimum Fano factor possible for spin-degenerate transport and thus suggest a spin-polarisation of the current.

5. Related work

5.1. Noise measurements in mechanically controlled break-junction setups

In a mechanically controlled break-junction (MCBJ) setup a piezo electric element is used to bend and tear apart a notched crystal. The contact that is formed between the two parts of the crystal just before it breaks is taken to be a single atom contact. Measurements using the MCBJ method are easier to perform compared to STM based measurements since contacts can be formed more rapidly and complete measurement cycles – including the noise measurements – can in principle be completely automated. In comparison with contacts formed inside a break-junction setup STM measurements have two main advantages. First, the atomic contact geometry can be determined and controlled by scanning the surface instead of the indirect methods like spectroscopy and conductance histograms used in MCBJ setups. Second, inhomogeneous systems can be created in a controlled fashion by evaporating either atoms, molecules or both onto a surface that has been verified to be flat and clean. The atoms type can be identified by either dI/dV measurements or apparent height comparison. Furthermore, the sample's surface geometry as well as the adatom to be contacted can be thoroughly examined both before and after the contact is established. The STM thus provides a high degree of control of the examined systems and it leaves the tip geometry as the main unknown in the setup.

Measurements of shot noise at single atom contacts in an MCBJ setup were first reported by van den Brom et al. [3]. The single atom contacts formed by bending and breaking a notched flat Au crystal were subject to shot noise measurements using an electronic noise measurement setup comparable to the setup described in this thesis. For contacts with conductances between $\approx 0.5\,G_0$ and $1\,G_0$ Fano factors were obtained that are consistent with a single spin degenerate transport channel. These findings are in line with the results of shot noise measurements at single Au adatoms on a Au(111) surface presented in this thesis. Contacts with

conductances between $1\,G_0$ and $2\,G_0$ show Fano factors that can be described by one fully transmissive spin degenerate channel and a combination of two channels that constitute the remaining conductance and keep a constant transmission ratio of 10%. Measurements at conductances above $2\,G_0$ scatter considerably and require at least two conductance channels.

The shot noise generated by electronic transport through a single deuterium D_2 molecule contacted by two Pt electrodes was measured by Djukic et al. [46]. After verifying the formation of a clean Pt contact with a characteristic conductance of $1.5\,G_0$ in their MCBJ setup, D_2 (or H_2) was injected into the chamber. The presence of D_2 in the junction was verified using conductances histograms. For two Pt-D_2-Pt contacts with conductances $1.010\,G_0$ and $0.98\,G_0$ Fano factor 0.02 and 0.03 were obtained, respectively. This shot noise suppression suggests the transport to be governed almost exclusively by a single fully transmissive spin degenerate transport channel. The result is consistent with DFT-calculations of a single D_2 molecule in linear arrangement [47, 48].

To follow up the initial publication on Au contacts [3] Kumar et al. [4] formed chains of Au atoms in an MCBJ setup and found signs of inelastic scattering at vibrational modes of the atomic chain in the shot noise measurements. Contacts consisting of 3–5 Au atoms were formed. Shot noise measurements were performed at the contacts and at low bias currents the excess noise increased with the applied current as expected from the Lesovik expression 2.16. The Fano factors were consistent with a single spin-degenerate transport channel. At bias voltages between 10 and 20 mV the linear increase of the noise density with the applied bias changed in slope by up to $\pm 10\%$. This slope change and an associated dip in the differential conductance of 1% at the same voltage is interpreted as the result of inelastic scattering at longitudinal vibrational modes of the Au chains.

Subsequent to the publication on spin polarised transport by the author of this thesis Vardimon et al. [5] found indication of complete spin filtering in nickel oxide contacts. In an MCBJ setup the authors formed single atom nickel contacts that show characteristic conductances around $2 - 4\,G_0$. After introducing oxygen to the junction the junctions sustained significantly longer elongations than the pure nickel contacts. During the elongation the conductance plateaus of pure nickel contacts were followed by conductances below $1\,G_0$ that are interpreted as the formation of NiO. Shot noise measurements performed on the later showed a spin polarisation of $> 90\%$ in 9% of the contacts. Calculations for geometrically

symmetric Ni-NiO-Ni junctions yielded two spin-degenerate states. The authors therefore argue that the single spin channel observed is due to less symmetric junction configurations in the experiments.

In an attempt to form contacts that show spin-polarised transport Kumar et al. [49] examined atomic chains based on Fe and Ni, that formed using deuterium molecules as a stabilisation. The combinations of conductance and Fano factor are not in the region forbidden for spin-degenerate transport. The authors argue that this does not exclude a spin-polarisation of the transport channels.

In further studies shot noise measurements were applied in MCBJ setups to deduce information on the zig-zag shape of Au atomic chains [50] and to infer reduced sets of possible transmission probabilities matching a certain combination of F and G [51]. All publications discussed in this section could benefit from the higher degree of control of the actual atomic geometry provided by STM.

5.2. Noise measurements in STM

Publications on shot noise measurements inside an STM are scarce and restricted to contact conductances significantly below those examined in this thesis. To the best of my knowledge the shot noise measurements presented in this thesis are the first to be performed at covalently bonded atomic contacts inside an STM.

The first measurements of shot noise in an STM were performed by Birk et al. [52] on single and double tunnel barriers. To form the double barrier tunnel junction (DBTJ) the authors grew Zr-oxide islands on a Au(111) substrat and covered them with a discontinuous gold film. By positioning a tip in tunnelling range above or between these islands the authors formed a double or a single tunnel barrier, respectively. For single tunnel barriers full poissonian shot noise $F = 1$ is observed, while for DBTJs the observed behaviour of the shot noise depends on the resistances of the two barriers R_1 and R_2 and their capacitances C_1 and C_2. For rather symmetric DBTJs the shot noise is suppressed in accordance with $S_I = S_{\mathrm{Poisson}}(R_1^2 + R_2^2)/(R_1 + R_2)^2$ down to a minimum of 1/2 if $R_1 = R_2$. For strongly asymmetric junctions ($R_1 \ll R_2$) the I/V curves acquired at the DBTJs show a stairlike behaviour that is indicative of coulomb blockade. In figure 5.1 the dependence of voltage and noise density on the current is shown from [52] that was acquired by Birk et al. in the coulomb blocking regime. In the upper part of the current-voltage curve is shown while the lower part displays the dependence of the Fano factor with the current. In an ideal model of

coulomb blocking a current is allowed to flow only if $|V| \geq \frac{E_C}{e} = \frac{e}{2C}$, with E_C being the energy needed to charge the state between the two tunnelling barriers with a single electron facing a capacitance of C. If $|V|$ differs from $\frac{E_C}{e}$ (mark A in figure 5.1) each electron that tunnels through R_1 enlarges the charge on the island and blocks further transmissions via R_1 until an electron leaves the island over R_2. The transport statistics is thus completely determined by the transmission over R_2 and full poissonian shot noise is both expected and measured. If $|V| = \frac{E_C}{e}$ (mark B in figure 5.1) the tunnelling between left electrode and the island and between the island and the right electrode is expected to occur in a alternated and thus correlated way. This leads to a shot noise reduction with a lower boundary of $\frac{1}{2}S_{\text{Poisson}}$.

While the experiments performed in [52] validates theoretical predictions [53] they are different from the work presented in this thesis. The latter were performed in contact to single atoms with conductances between $0.4 - 1\,\text{G}_0$ while the former yielded conductances $\leq 1/(1\,\text{G}\Omega)$.

In a publication by Herz et al. [7], the current noise was measured while scanning with an Ir tip over an Ir defect structure that was formed by repeatedly indenting the tip into the sample. During this preparation procedure random occurances of "subatomic structures" [7] emerged in the topographs. While scanning over a defect structure Fano factors of 1.13 ± 0.26 independent on the lateral position were determined from current noise measurements. The tunnelling resistance during these scans was $77\,\text{M}\Omega$ corresponding to $1.7 \cdot 10^{-4}\,G_0$. This result is in line with the theory that yield an asymptotic Fano factor $F = 1$ for small conductances. In comparison, the work presented in this thesis has the possibility to prepare and verify flat surfaces as well as to identify and contact single adatom species with confidence. Furthermore it shows the first measurements in covalent contact to adatom in contrast to the tunnelling range used in [7]

Kemiktarak et al. [8, 54] demonstrated the measurement of both displacement and shot noise in a tunnelling contact inside an STM utilising radio frequency (RF) signals. To measure the displacement or conductance the tunnelling contact was incorporated into an LC resonant circuit. The impedance of the resonant circuit combined with the tunnelling conductance was measured using radio-frequency reflectometry and it can be mapped to the tunnelling conductance. The advantage of this method over the direct current measurement is the higher bandwidth that is limited only be the 2 MHz bandwidth of the resonant circuit. To perform the noise measurements the authors placed a cryogenic RF-amplifier

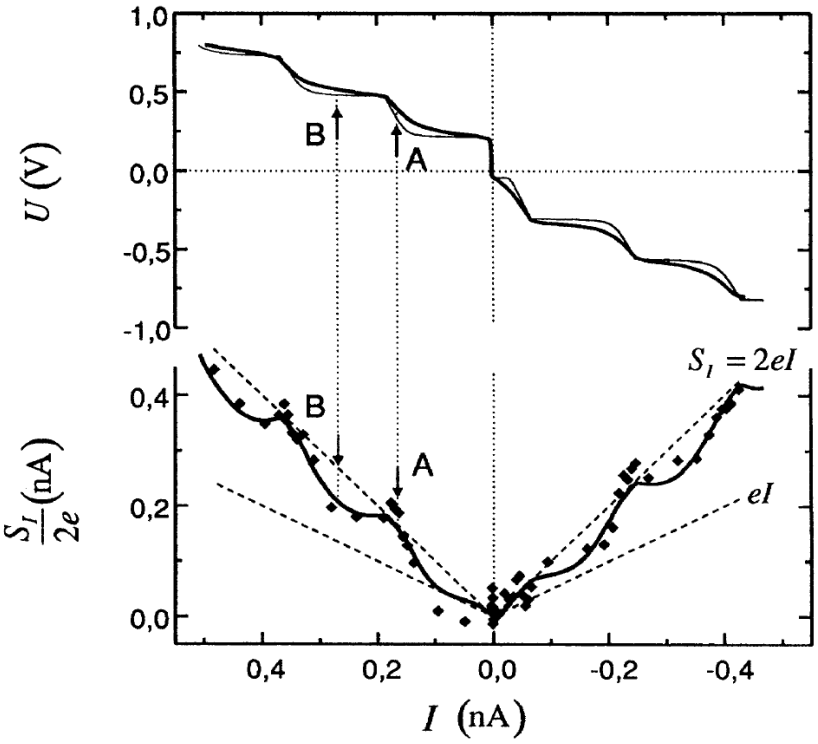

Figure 5.1.: Dependence of voltage and current noise density on the current measured at an asymmetric double barrier tunnel junction in an STM at 4.2 K. Coulomb blockade results in a stairlike V/I curve as well as a suppression of the shot noise for $|V| \neq \frac{E_C}{e}$ (A) and $|V| = \frac{E_C}{e}$ (B). E_C is the charging energy of the state on the island. See text for details and discussion. Source: [52]

adjacent to the contact was used to amplify the noise from the resonant circuit [1] which in turn was powered by the noise originating from the tunnelling contact. After calibrating this setup by varying the temperature shot noise measurement were performed at contacts ranging from 300 kΩ to 3 MΩ and at temperatures between 4 K and 300 K on a Au sample. All measurements presented by the authors show full poissonian shot noise and a temperature dependent flattening at low biases fitting the theoretical expectations of the Lesovik expression 2.16.

The high measurement frequency of 223 MHz used by Kemiktarak et al. [8, 54] has several advantages over noise measurements in the kilohertz range as performed in this thesis. First, it is well above the low frequency noise component that forms a lower limit to the frequency interval usable for evaluation and thus allows for measurements at higher biases. Second, the acquisition time for a single noise measurements is in the millisecond range as compared to several

[1] $f_{LC} \approx 223$ MHz, bandwidth ≈ 10 MHz

minutes required in the approach used in this work. The conductance of the contacts examined by Kemiktarak et al. however is $< 0.043\,G_0$ and thus much less than the conductances of the covalently bonded contacts examined in this thesis. Furthermore, although the topographs of a Au surface showed terraces no claims as to the precision and stability of the STM was made.

6. Discussion

In order to investigate the underlying causes of the observed spin polarisation of the transport channels for the transport through some of the examined single Fe and Co adatoms on Au(111) this chapter starts with a discussion on the involved atomic orbitals based on symmetry. The results of the discussion are further corrobated by spin-polarised density-functional-theory (SPDFT) calculations in the second part 6.3.

6.1. Transport channels and atomic orbital symmetry

The observation of spin-polarisation of the transport channels for some of the contacts to Fe and Co adatoms was not anticipated, even though both Fe and Co are paramagnetic atoms. The high valency of the two atomic species was previously thought to lead to a large number of transport channels involved [55] which in turn would increase the Fano factor considerably. Yet this is contrary to the measurement results for Fe.

To find a reason for the low number of involved channels and their spin polarisation we consider the overlap of the Au tip apex atom's s-orbital and the orbitals of the Fe or Co adatom. The s-orbital has a radial symmetry that yields considerable overlap with the s-, p_z- and d_{z^2}-orbitals of the adatom it is in contact with. The coupling of the s-orbital with the other p and d orbitals of the adatom ($d_{xy}, d_{xz}, d_{yz}, d_{x^2-y^2}, p_x, p_y$) is strongly suppressed by symmetry. Thus, the s-orbital of the tip apex Au atom acts as an orbital filter [56]. This reduces the number of atomic orbitals available for the formation of transport channels. The observation of spin-polarisation of the transport channels is further deduced by SPDFT-calculations in the subsection 6.3.

6.2. Electronic transport and Kondo effect

Co adatoms on a Au(111) surface show a Kondo effect [45]. In the preceding sections the shot noise measurements at Co adatoms on the Au(111) surface where interpreted using the scattering picture of electronic transport. Based on that model a spin-polarisation was suggested for one of the measurements. The Kondo effect was not taken into account in that interpretation.

To the best of my knowledge, no theoretical assessments exist for the shot noise generated by the transport through single atoms exhibiting a Kondo resonance. For transport through mesoscopic quantum dots showing a Kondo resonance the generated shot noise has been studied [57, 58, 59]. Since a discussion on the transferability of these theoretical models to the transport through single atoms is beyond the scope of this thesis it is only noted here that the screening of the local magnetic moment by the conduction band electrons need not be complete. Such an underscreening was shown for Co atoms in molecules contacted by two Au electrodes [60]. Since an underscreened system retains a net spin moment it could reconcile the suggested spin-polarisation of the transport channels for measurement A in section 4.6 with the presence of a Kondo effect.

6.3. Comparison with DFT-based transport calculations

In order to shed some first light onto the underlying microscopic transport mechanisms of the Co/Au(111) and the Fe/Au(111) systems, transport calculations based on spin-polarised density functional theory (SPDFT) calculations were performed by Mads Brandbyge at the Department of Micro- and Nanotechnology of the Technical University of Denmark. While the calculations were not performed by the author of this thesis, the results are included here to discuss the relevant electronic orbitals involved in the transport process of the examined systems and to corrobate the interpretation given in section 6.1.

In the first step SPDFT calculations were performed on a geometry that consisted of 12 layers of Au(111) in a 4×4 atomic surface unit-cell with a Co/Fe atom adsorbed in fcc position contacted by a tip constructed of 4 atoms. The geometry is depicted in the inset of figure 6.1. The GGA-PBE exchange-correlation functional [61], a localized atomic orbital basis set (SIESTA) [62] and a 3×3 surface k-point sampling were used. Based on the results of the SPDFT calculations the transmission matrix $\mathbf{t}$ was calculated using the TranSIESTA setup [63]. There, the Kohn-Sham wave functions of the SPDFT calculations are used as real single-particle wave functions in a non-equilibrum Green's-function formalism. Within that formalism the transmission matrix $\mathbf{t}$ is computed. For each k-point and each spin direction σ the eigenvectors and eigenvalues of $\mathbf{t}$ are the transport eigenchannels and their associated transmission probabilities $\tau_{\sigma i}(k)$, respectively.

In calculating the Fano factor from the $\tau_{\sigma i}(k)$ the way of averaging over the k-points becomes important. For a discussion on the subtleties of the k-point averaging the reader is referred to the supplementary information of [64]. In summary two schemes are used: In the first one the periodic-boundary-conditions (PBC) of the DFT super-cell lead to contributions to the Fano factor of neighbouring repetitions of the super-cell. In the single-atom (SA) scheme this inter-super-cell effect is diminished.

The method is subject to the approximations inherent in DFT, the exchange-correlation functional and the use of the Kohn-Sham wavefunctions as real-world wave functions and as a basis for the transport calculations. In particular, it does not describe many-body effects, e.g. the Kondo effect, or inelastic phonon scattering.

The calculations were performed for a set of 5 tip-adatom distances[1] to account for the spread in the experimental conductances. In figure 6.3 the calculated Fano factors and conductances are compared to the experimental data for Fe/Au(111) and Co/Au(111). The results reproduce the experimental data well, except for the Co/Au(111) simulation using the single atom (SA) method of k-point averaging. It shows an almost vanishing spin-polarisation of the transport channels while some of the experimental data acquired at Co/Au(111) suggests a spin-polarisation. Since the simulation does not include Kondo physics this is not surprising, see section 6.2.

Figure 6.1 shows the energy dependence of the Fano factor, the conductance and the transmissivity of spin majority and minority for (a) Fe/Au(111) and (b) Co/Au(111). The data was determined using periodic-boundary-condition k-point averaging and a tip-sample distance of $d = 3.85$. The values at E_F should be compared to the experimental low-bias data. The calculations show that for each spin direction a single channel is dominating the transport through the adatom in both the Fe/Au(111) and the Co/Au(111) system. The dominating spin polarised channel is rotationally symmetric around the surface normal (Γ_1 symmetry). In terms of atomic orbitals the s, p_z and d_{z^2} orbitals at the adatom share this geometry and can thus contribute to the transport. The Au atom's s valency orbital has Γ_1 symmetry. The coupling of this s orbital with $d_{xy}, d_{xz}, d_{yz}, d_{x^2-y^2}, p_x$ or p_y will be suppressed by symmetry leaving only the rotationally symmetric orbitals. The Au atom thus acts as an orbital filter.

To further corroborate the Γ_1 symmetry, the wave functions constituting the dominating transport eigenchannel are shown in figure 6.2. For the spin-minority of (a) Fe/Au(111) and (b) Co/Au(111) the isosurfaces of the real part of the dominant eigenchannel of $\mathbf{t}$ are rendered for a positive (red) and a negative (blue) value. Using this way of rendering the symmetry of the wave function becomes visible. In both cases the isosurface representation of the dominating transport eigenchannel shows a rotational symmetry around the z-axis. Additionally, for the Co adatom (b) the isosurfaces show a resemblance with a d_{z^2} orbital. This is consistent with DFT calculations on Cu/Co/Cu contacts [65] that showed a dominating Γ_1 channel in the tunneling and weak contact regimes.

Finding a single dominant transport channel for spin up with transmissivity $\tau_\uparrow$ a second for spin down with transmissivity $\tau_\downarrow$ allows for the determination of the spin polarisation $P = (\tau_\uparrow - \tau_\downarrow)/(\tau_\uparrow + \tau_\downarrow)$ from the experimental data. For a

[1] For Fe/Au(111): $d = 3.70...4.10$ Å , for Co/Au(111): $d = 3.85...4.25$ Å

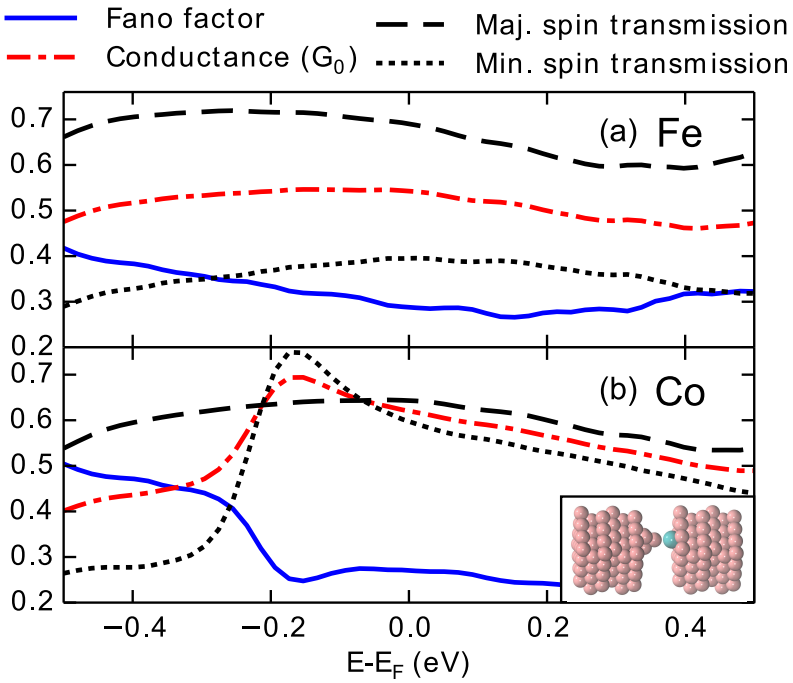

Figure 6.1.: Results of transport calculations for the structure shown in the inset for an Fe adatom (upper panel) and a Co adatom (lower panel) at $d = 3.85$ using periodic boundary conditions in the surface. The energy-resolved conductances in units of G_0, k-point averaged Fano factors and transmissions of majority and minority spin channels are shown as dash dotted, solid, dashed, and dotted lines. The values at E_F should be compared to the experimental low-bias data. (*Copyright 2015 American Physical Society, reprinted with permission from* [64])

single channel and a fixed polarisation Fano factor and conductance have a linear dependence. In figure 6.3 the dashed grey lines show this linear dependence for spin polarisations $P = 20\%$, $P = 40\%$, $P = 60\%$ and $P = 80\%$. For a multi-channel scenario these lines represent the lower boundaries of the spin-polarisation. Spin polarisations up to 50% and 40% can be determined from experimental data measured at Fe/Au(111) and Co/Au(111), respectively.

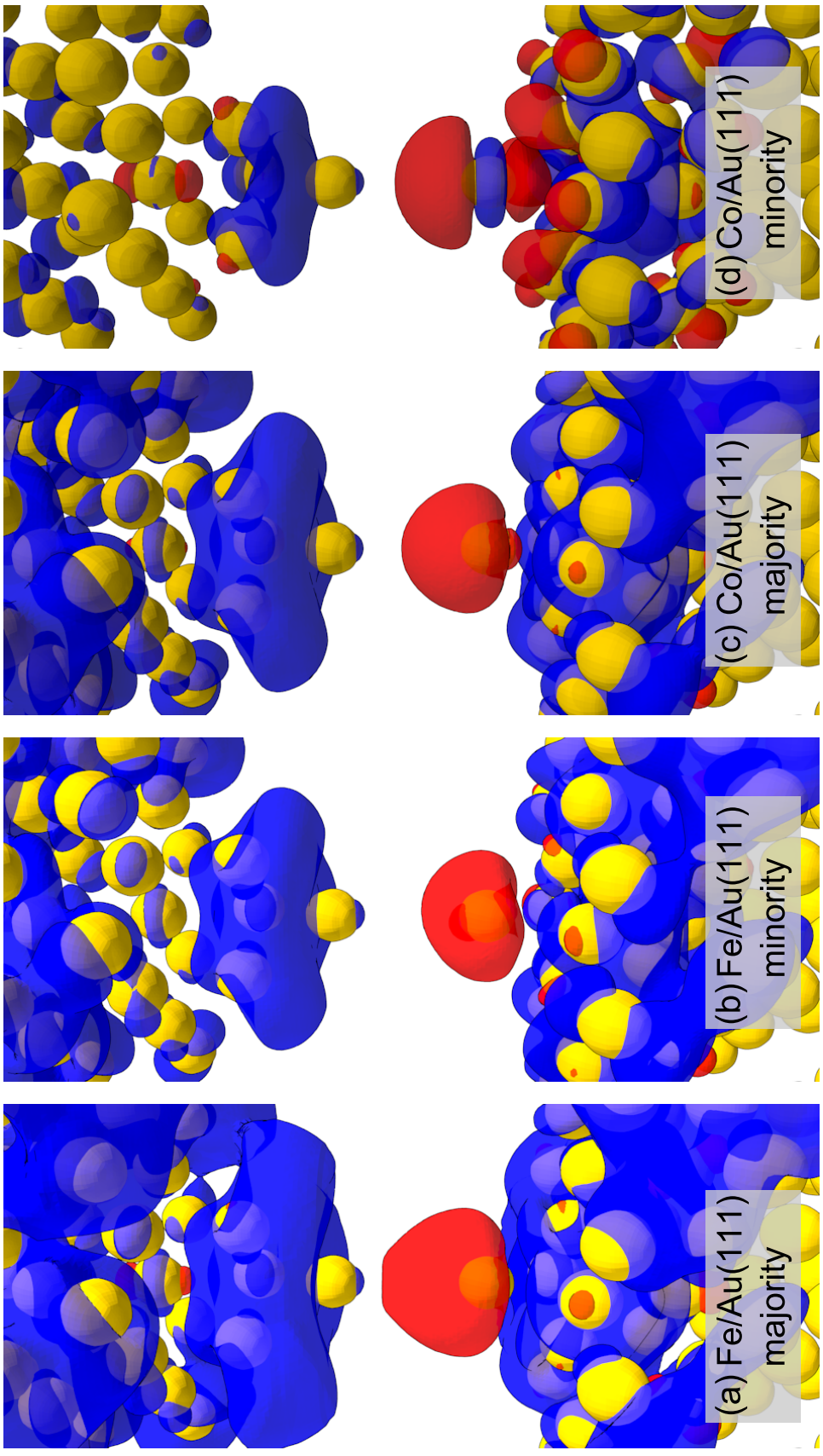

Figure 6.2.: Isosurface renderings dominating eigenchannel for (a) Fe/Au(111) spin majority, (b) Fe/Au(111) spin minority, (c) Co/Au(111) spin majority and (d) Co/Au(111) spin minority. For the dominating eigenchannel the real part of the wavefunction is shown for a positive value (red) and a negative value (blue). In all cases shown the dominating eigenchannel is rotationally symmetric around the surface normal at the position of the adatom.

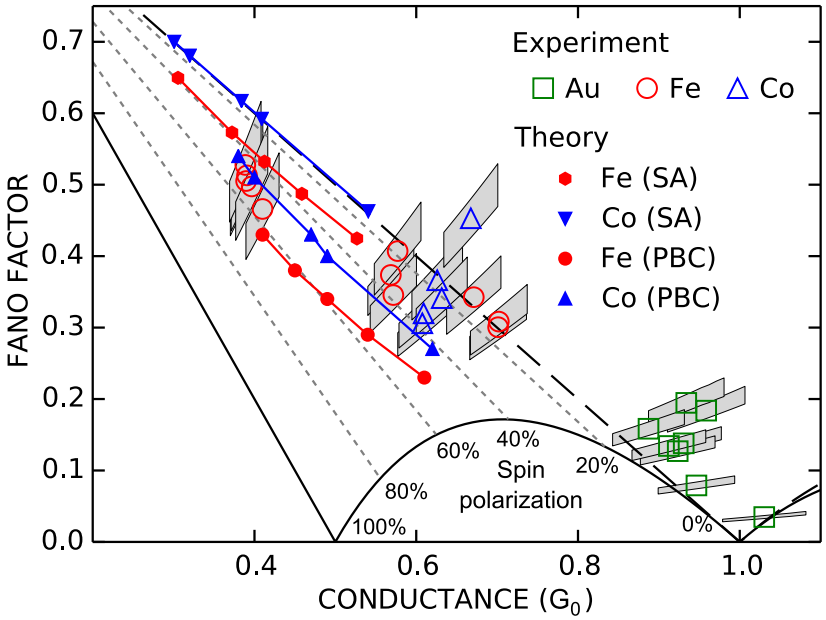

Figure 6.3.: Experimental Fano factors and conductances are shown for all stable Au/Fe/Co contacts on the Au(111)-surface. Theoretical values determined for Fe/Au(111) and Co/Au(111) system are shown for the single-atom (SA) and periodic-boundary-conditions (PBC) method of k-point averaging (as defined in the text) and for 5 tip-adatom distances (Fe/Au(111): d = 3.70...4.10 Å , Co/Au(111): d = 3.85...4.25 Å), each. Black dashed (solid) line shows the minimum Fano factor possible for spin-degenerate (spin-polarised) transport. Dashed grey lines indicate the constraints on Fano factor and conductance for a single channel with polarisations $P = 20\%$, $P = 40\%$, $P = 60\%$ and $P = 80\%$. (*Copyright 2015 American Physical Society, reprinted with permission from* [64])

7. Conclusion and outlook

An experimental setup to measure shot noise at atomic contacts formed inside an STM was built and put into operation. Shot noise measurements were successfully performed at contacts to single Au, Fe and Co adatoms on a Au(111) surface. For some contacts to Fe and Co adatoms the shot noise measurements showed evidence of a spin-polarisation of the transport channels. This proves the unique value of shot noise measurements in probing spin-polarisation without requiring a spin-polarisation of either tip or sample. It thus provides valuable information on the transport process of heterogenous single atom systems not attainable through other measurement techniques.

Combining the high degree of control the STM offers and the capabilities of shot noise measurements to gain valuable information on the transport process yields a powerful means to analyse the electronic transport through a virtually unlimited variety of atomic and molecular contact systems. Each of these systems can contain one or more of the most prominent and complex effects in multi particle solid state physics. The following few examples highlight the potential of the method.

Several variations and extensions of the systems examined in this thesis lend themselves for future examination. First, the exact requirements for the contacts to Fe and Co on Au(111) to show spin-polarisation could be addressed in particular with regards to their position on the Au(111) herring-bone reconstruction. Second, the interaction between the spin-polarisation of the transport channels in contact to one adatom and spin structures in the vicinity could be examined. These spin structures can be other magnetic single adatoms, chains, cluster or islands. Third, the transport behaviour of contact geometries involving more than one magnetic atom is of interest. Examples are vertical dimers formed by picking up one magnetic atom to the tip and contacting a second one, or contacts to dimers on the surface. Finally, for contacts that involve a known spin-polarisation of either the tip, sample or both it will be interesting to bring into congruence a possible spin-polarisation obtained from the shot noise measurements with the spin-polarisation of the contact components determined

using different measurement techniques, e.g. light emission.

The effect of superconductivity in either sample, tip or both on the transport through single atom contacts is of particular interest to the author. At the interface between superconducting and normal metal material the charge carrier statistics is governed by Andreèv reflections leading to a distinct behaviour of the shot noise [17]. While experimental verification of the particle statistics has been performed for contacts at mesoscopic scales, atomic scale systems have evaded analysis so far. Shot noise measurements thus provide a unique possibility to put the established theory for electronic transport through single atom contacts to the test.

Acknowledgements

The work presented in this thesis would not have been possible without the help and support by the following persons.
First, I'd like to thank Prof. Dr. Richard Berndt for suggesting the experiment and giving me the freedom to pursue it in my own way in his well equipped laboratories. He supported my work with technical expertise and followed its progress with endless patience.
I thank Alexander Weismann for supervising the project and supporting it with key improvements to the STM as well as technical and theoretical ideas.
The project would not have been successful without the help of Hans-Joachim Neumann. He built the symmetric transmission devices that were pivotal for the successful shot noise measurements. I am indepted to him for his patience in discussing electronic issues and rescuing me from getting lost in electronic peculiarities.
I'd like to express my gratitude to Mads Brandbyge for performing and discussing the transport calculations.
I thank Manuel Gruber for his excellent comments and the time taken to proofread the manuscript.
Further I'd like to thank:

- Johannes Schöneberg for a comfortable office climate and fruitful discussions.
- Peter-Jan Peters for joint meanderings through the thicket of transport and shot noise theory.
- Renè Woltmann and Daniel Striezel for building the casings for the electronics.
- Monika Seeger for taking on administrational tasks in her cheerful way.
- all my colleagues and former coworkers in the group of Richard Berndt.

I am deeply thankful to my parents for their unconditional support and for bearing with me through the hard times.

Glossary

DBTJ . . . . . double barrier tunnel junction

DFT . . . . . density functional theory

fcc . . . . . face-centered-cubic

hcp . . . . . hexagonal-close-packed

HF . . . . . high frequency

LDOS . . . . . local density-of-states

MCBJ . . . . . mechanically controlled break-junction

PBC . . . . . periodic-boundary-conditions, a scheme of k-point averaging

RKKY . . . . . Ruderman-Kittel-Kasuya-Yosida

SA . . . . . single atom scheme of k-point averaging

SMD . . . . . surface-mount device

SPDFT . . . . . spin-polarised density-functional-theory

STM . . . . . scanning tunnelling microscope

Bibliography

[1] J. Kröger, N. Néel, and L. Limot, "Contact to single atoms and molecules with the tip of a scanning tunnelling microscope", Journal of Physics: Condensed Matter **20**, 223001 (2008).

[2] A. Kumar, L. Saminadayar, D. C. Glattli, Y. Jin, and B. Etienne, "Experimental Test of the Quantum Shot Noise Reduction Theory", Phys. Rev. Lett. **76**, 2778 (1996).

[3] H. E. van den Brom and J. M. van Ruitenbeek, "Quantum Suppression of Shot Noise in Atom-Size Metallic Contacts", Phys. Rev. Lett. **82**, 1526 (1999).

[4] M. Kumar, R. Avriller, A. L. Yeyati, and J. M. van Ruitenbeek, "Detection of Vibration-Mode Scattering in Electronic Shot Noise", Phys. Rev. Lett. **108**, 146602 (2012).

[5] R. Vardimon, M. Klionsky, and O. Tal, "Indication of Complete Spin Filtering in Atomic-Scale Nickel Oxide", Nano Letters **15**, 3894 (2015).

[6] H. Birk, M. J. M. de Jong, and C. Schönenberger, "Shot-Noise Suppression in the Single-Electron Tunneling Regime", Phys. Rev. Lett. **75**, 1610 (1995).

[7] M. Herz, S. Bouvron, E. Cavar, M. Fonin, W. Belzig, and E. Scheer, "Fundamental quantum noise mapping with tunnelling microscopes tested at surface structures of subatomic lateral size", Nanoscale **5**, 9978 (2013).

[8] U. Kemiktarak, T. Ndukum, K. C. Schwab, and K. L. Ekinci, "Radio-frequency scanning tunnelling microscopy", Nature **450**, 85 (2007).

[9] C. J. Chen, "Introduction to Scanning Tunneling Microscopy", 2nd ed. (Oxford University Press, 2008).

[10] J. Bardeen, "Tunnelling from a Many-Particle Point of View", Phys. Rev. Lett. **6**, 57 (1961).

[11] J. Tersoff and D. R. Hamann, "Theory and Application for the Scanning Tunneling Microscope", Phys. Rev. Lett. **50**, 1998 (1983).

[12] J. Tersoff and D. R. Hamann, "Theory of the scanning tunneling microscope", Phys. Rev. B **31**, 805 (1985).

[13] R. Feenstra, J. A. Stroscio, and A. Fein, "Tunneling spectroscopy of the Si(111)2 × 1 surface", Surface Science **181**, 295 (1987).

[14] S. Kogan, "Electronic Noise and Fluctuations in Solids" (Cambridge University Press, 2008).

[15] Y. Imry, "Introduction To Mesoscopic Physics" (Oxford University Press, 1997).

[16] Y. Blanter and M. Büttiker, "Shot noise in mesoscopic conductors", Physics Reports **336**, 1 (2000).

[17] N. Agraït, A. L. Yeyati, and J. M. van Ruitenbeek, "Quantum properties of atomic-sized conductors", Physics Reports **377**, 81 (2003).

[18] R. Landauer, "Spatial variation of currents and fields due to localized scatterers in metallic conduction (and comment)", Journal of Mathematical Physics **37**, 5259 (1996).

[19] P. Horowitz and W. Hill, "The Art Of Electronics", 2nd ed. (Cambridge University Press, 1991).

[20] S. L. Bittel H., "Rauschen" (Springer-Verlag Berlin, 1971).

[21] U. Gavish, "Quantum Current Noise in Mesoscopic Systems", Ph.D. thesis, Weizmann Insitute of Science (2003).

[22] H. Nyquist, "Thermal Agitation of Electric Charge in Conductors", Phys. Rev. **32**, 110 (1928).

[23] W. Schottky, Ann. Phys. **362**, 541 (1918).

[24] T. Martin and R. Landauer, "Wave-packet approach to noise in multichannel mesoscopic systems", Phys. Rev. B **45**, 1742 (1992).

[25] R. Landauer and T. Martin, "Equilibrium and shot noise in mesoscopic systems", Physica B: Condensed Matter **175**, 167 (1991).

[26] G. B. Lesovik, Sov. Phys. JETP Lett. **49**, 592 (1989).

[27] K. Thibault, J. Gabelli, C. Lupien, and B. Reulet, "Pauli-Heisenberg Oscillations in Electron Quantum Transport", Phys. Rev. Lett. **114**, 236604 (2015).

[28] N. L. Schneider, G. Schull, and R. Berndt, "Optical Probe of Quantum Shot-Noise Reduction at a Single-Atom Contact", Phys. Rev. Lett. **105**, 026601 (2010).

[29] N. L. Schneider, "Noise properties of atomic-size contacts" (2013).

[30] E. Rubiola and F. Vernotte, "The cross-spectrum experimental method", .

[31] C. Boggs, A. Doak, and F. Walls, "Measurement of voltage noise in chemical batteries", in "Frequency Control Symposium, 1995. 49th., Proceedings of the 1995 IEEE International" (1995) pp. 367 –373.

[32] R. Morrison, "Grounding and shielding techniques in Instrumentation" (John Wiley & Sons, Inc., 1986).

[33] A. Sperl, J. Kröger, and R. Berndt, "Direct observation of conductance fluctuations of a single-atom tunneling contact", Phys. Rev. B **81**, 035406 (2010).

[34] N. Agraït, J. G. Rodrigo, and S. Vieira, "Conductance steps and quantization in atomic-size contacts", Phys. Rev. B **47**, 12345 (1993).

[35] M. L. Trouwborst, E. H. Huisman, F. L. Bakker, S. J. van der Molen, and B. J. van Wees, "Single Atom Adhesion in Optimized Gold Nanojunctions", Phys. Rev. Lett. **100**, 175502 (2008).

[36] J. V. Barth, H. Brune, G. Ertl, and R. J. Behm, "Scanning tunneling microscopy observations on the reconstructed Au(111) surface: Atomic structure, long-range superstructure, rotational domains, and surface defects", Phys. Rev. B **42**, 9307 (1990).

[37] F. Libisch, V. Geringer, D. Subramaniam, J. Burgdörfer, and M. Morgenstern, "Diffractive-wave guiding of surface electrons on Au(111) by the herringbone reconstruction potential", Phys. Rev. B **90**, 035442 (2014).

[38] W. Chen, V. Madhavan, T. Jamneala, and M. F. Crommie, "Scanning Tunneling Microscopy Observation of an Electronic Superlattice at the Surface of Clean Gold", Phys. Rev. Lett. **80**, 1469 (1998).

[39] A. Castellanos-Gomez, G. Rubio-Bollinger, M. Garnica, S. Barja, A. L. V. de Parga, R. Miranda, and N. Agraït, "Highly reproducible low temperature scanning tunneling microscopy and spectroscopy with in situ prepared tips", Ultramicroscopy **122**, 1 (2012).

[40] V. Madhavan, W. Chen, T. Jamneala, M. F. Crommie, and N. S. Wingreen, "Tunneling into a Single Magnetic Atom: Spectroscopic Evidence of the Kondo Resonance", Science **280**, 567 (1998).

[64] A. Burtzlaff, A. Weismann, M. Brandbyge, and R. Berndt, "Shot Noise as a Probe of Spin-Polarized Transport through Single Atoms", Phys. Rev. Lett. **114**, 016602 (2015).

[41] M. A. Ruderman and C. Kittel, "Indirect Exchange Coupling of Nuclear Magnetic Moments by Conduction Electrons", Phys. Rev. **96**, 99 (1954).

[42] T. Kasuya, "A Theory of Metallic Ferro- and Antiferromagnetism on Zener's Model", Progress of Theoretical Physics **16**, 45 (1956).

[43] K. Yosida, "Magnetic Properties of Cu-Mn Alloys", Phys. Rev. **106**, 893 (1957).

[44] L. Zhou, J. Wiebe, S. Lounis, E. Vedmedenko, F. Meier, S. Blügel, P. H. Dederichs, and R. Wiesendanger, "Strength and directionality of surface Ruderman-Kittel-Kasuya-Yosida interaction mapped on the atomic scale", Nature Physics **6**, 187 (2010).

[45] V. Madhavan, W. Chen, T. Jamneala, M. F. Crommie, and N. S. Wingreen, "Local spectroscopy of a Kondo impurity: Co on Au(111)", Phys. Rev. B **64**, 165412 (2001).

[46] D. Djukic and J. M. van Ruitenbeek, "Shot Noise Measurements on a Single Molecule", Nano Letters **6**, 789 (2006).

[47] K. S. Thygesen and K. W. Jacobsen, "Conduction Mechanism in a Molecular Hydrogen Contact", Phys. Rev. Lett. **94**, 036807 (2005).

[48] V. M. García-Suárez, A. R. Rocha, S. W. Bailey, C. J. Lambert, S. Sanvito, and J. Ferrer, "Single-channel conductance of H_2 molecules attached to platinum or palladium electrodes", Phys. Rev. B **72**, 045437 (2005).

[49] M. Kumar, K. K. V. Sethu, and J. M. van Ruitenbeek, "Molecule-assisted ferromagnetic atomic chain formation", Phys. Rev. B **91**, 245404 (2015).

[50] R. Vardimon, T. Yelin, M. Klionsky, S. Sarkar, A. Biller, L. Kronik, and O. Tal, "Probing the Orbital Origin of Conductance Oscillations in Atomic Chains", Nano Letters **14**, 2988 (2014).

[51] R. Vardimon, M. Klionsky, and O. Tal, "Experimental determination of conduction channels in atomic-scale conductors based on shot noise measurements", Phys. Rev. B **88**, 161404 (2013).

[52] H. Birk, M. J. M. de Jong, and C. Schönenberger, "Shot-Noise Suppression in the Single-Electron Tunneling Regime", Phys. Rev. Lett. **75**, 1610 (1995).

[53] S. Hershfield, J. H. Davies, P. Hyldgaard, C. J. Stanton, and J. W. Wilkins, "Zero-frequency current noise for the double-tunnel-junction Coulomb blockade", Phys. Rev. B **47**, 1967 (1993).

[54] U. Kemiktarak, "Radio-Frequency Scanning Tunneling Microscopy: Instrumentation and Applications To Physical Measurements", Ph.D. thesis, Boston University (2005).

[55] E. Scheer, N. Agrait, J. C. Cuevas, A. L. Yeyati, B. Ludoph, A. Martin-Rodero, G. R. Bollinger, J. M. van Ruitenbeek, and C. Urbina, "The signature of chemical valence in the electrical conduction through a single-atom contact", Nature **394**, 154 (1998).

[56] J. Schöneberg, F. Otte, N. Néel, A. Weismann, Y. Mokrousov, J. Kröger, R. Berndt, and S. Heinze, "Ballistic Anisotropic Magnetoresistance of Single-Atom Contacts", Nano Letters **16**, 1450 (2016).

[57] E. Sela, Y. Oreg, F. von Oppen, and J. Koch, "Fractional Shot Noise in the Kondo Regime", Phys. Rev. Lett. **97**, 086601 (2006).

[58] K.-H. Yang, Y.-J. Wu, and Y. Chen, "AC shot noise through a quantum dot in the Kondo regime", Physics Letters A **375**, 3037 (2011).

[59] K. Walczak, "Spin-dependent shot noise of inelastic transport through molecular quantum dots", Journal of Magnetism and Magnetic Materials **305**, 475 (2006).

[60] Parks, J. J. and Champagne, A. R. and Costi, T. A. and Shum, W. W. and Pasupathy, A. N. and Neuscamman, E. and Flores-Torres, S. and Cornaglia, P. S. and Aligia, A. A. and Balseiro, C. A. and Chan and Abruna, H. D. and Ralph, D. C., "Mechanical Control of Spin States in Spin-1 Molecules and the Underscreened Kondo Effect", Science **328**, 1370 (2010).

[61] J. P. Perdew, K. Burke, and M. Ernzerhof, "Generalized Gradient Approximation Made Simple", Phys. Rev. Lett. **77**, 3865 (1996).

[62] J. M. Soler, E. Artacho, J. D. Gale, A. García, J. Junquera, P. Ordejón, and D. Sánchez-Portal, "The SIESTA method for ab initio order-N materials simulation", Journal of Physics: Condensed Matter **14**, 2745 (2002).

[63] M. Brandbyge, J.-L. Mozos, P. Ordejón, J. Taylor, and K. Stokbro, "Density-functional method for nonequilibrium electron transport", Phys. Rev. B **65**, 165401 (2002).

[65] M. Polok, D. V. Fedorov, A. Bagrets, P. Zahn, and I. Mertig, "Evaluation of conduction eigenchannels of an adatom probed by an STM tip", Phys. Rev. B **83**, 245426 (2011).

List of Figures

Appendix A.

Conductance from thermal noise

To determine the contact conductance from the thermal noise acquired at a contact consider the circuit depicted in figure A.1 (a). The atomic contact inside the STM has a conductance g_C and is at a temperature T_C. It is connected to the external circuit that is represented by a resistance with conductance g_R being at room temperature T_R. Since the voltage noise densities averaged in the intervall $1 - 3\,\mathrm{kHz}$ are used to determine the contact conductance the reduction of the external circuit to the DC case is valid.

In the following the dependence between the contact conductance g_C and the measured voltage noise density S_{VV} will be established. Both the contact and the external resistor generate thermal current noise densities $S_{II}^C = 4k_BT_Cg_C$ and $S_{II}^R = 4k_BT_Rg_R$, respectively. Since they are parallel to each other they add to a total current noise density $S_{II}^{\mathrm{tot}} = 4k_BT_Cg_C + 4k_BT_Rg_R$. This is related to the voltage noise density S_{VV} by the total conductance $g_{\mathrm{tot}} = g_C + g_R$:

$$S_{VV} = \frac{S_{II}}{g_{\mathrm{tot}^2}} = \frac{4k_B(T_Rg_R+T_Cg_C)}{(g_C+g_R)^2} = \frac{4k_B(T_Rg_R+T_Cg_C)}{g_C^2+2g_cg_R+g_R^2}$$

Solving the above equation for g_C yields the quadratic equation:

$$g_C^2 + (2g_R - \frac{4k_BT_C}{S_{VV}})g_C + g_R^2 - \frac{4kBT_Rg_R}{S_{VV}}$$

which has the positive solution

$$g_C = -g_R + \frac{2k_BT_C}{S_{VV}} + \sqrt{\left(g_R - \frac{2k_BT_C}{S_{VV}}\right)^2 - g_R^2 + \frac{4kBT_Rg_R}{S_{VV}}}$$

Additionally, an offset O was introduced to account for correlated parts of the cross spectral density not origination from the contact, e.g. the thermal noise

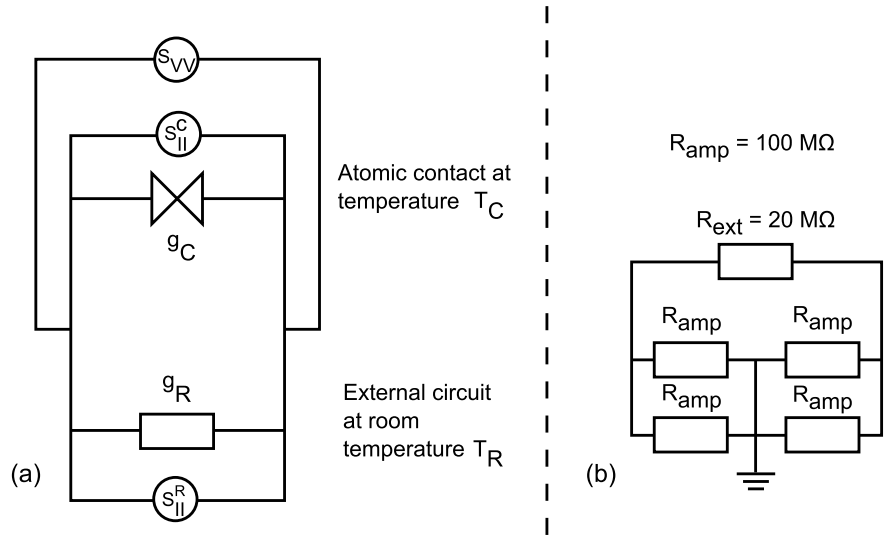

Figure A.1.: (a) Equivalent circuit for a contact indicated by the bow tie symbol being connected to an circuit external to the STM. The contact has a temperature T_C, a conductance g_C and generates a current noise power density S_{II}^C. The external circuit is represented by a resistance with conductance g_R being at a temperature T_R. S_{VV} is the voltage noise density that is measured across the contact and the external resistance in parallel. (b) The components constituting the external resistance. $R_{amp} = 100\,\mathrm{M\Omega}$ is the input resistance of the low-noise amplifiers and $R_{ext} = 20\,\mathrm{M\Omega}$ is the resistance of the low-noise current source as defined in figure 3.4. The circuit has a total resistance of $R_{ext} \parallel 100\,\mathrm{M\Omega}$.

from the cables connecting tip and sample with the feedthroughs.

$$g_C = -g_R + \frac{2k_BT_C}{S_{VV} - O} + \sqrt{\left(g_R - \frac{2k_BT_C}{S_{VV} - O}\right)^2 - g_R^2 + \frac{4kBT_Rg_R}{S_{VV} - O}}$$

The resistance of the setup outside of the STM was calculated from the parallel circuit of the $20\,\mathrm{M\Omega}$ input resistance of the low-noise amplifiers and The room temperature T_R was chosen as $300\,\mathrm{K}$. Its variation has negligible influence on the determined contact conductance. The contact temperature T_C was determined from a fit to the calibration data acquired according to section 3.3.4. With $T_C = 4.5\,\mathrm{K}$ and $O = 1.0441 \cdot 10^{-18}\frac{V^2}{\mathrm{Hz}}$ the conductances determined from the thermal noise fit the four-point conductance measurements to within 3.1%, as detailed in section 3.3.4.

Erklärung

Hiermit erkläre ich, dass ich diese Arbeit unter Einhaltung der Regeln guter wissenschaftlicher Praxis der Deutschen Forschungsgemeinschaft selbständig unter der Beratung meiner wissenschaftlichen Lehrer und nur mit den angegebenen Hilfsmitteln erstellt habe und dass sie nach Inhalt und Form meine eigene ist. Diese Arbeit wurde weder ganz noch in Teilen an anderer Stelle im Rahmen eines Prüfungsverfahrens vorgelegt.

Kiel, den _____ 2017

_____

(Andreas Burtzlaff)